Radio reflections in the atmosphere as potential background for radio detection of cosmic rays

Bachelor's Thesis in Physics

Presented by
Carina Kanitz
April 1, 2020

Erlangen Center for Astroparticle Physics
Friedrich-Alexander-Universität Erlangen-Nürnberg

Supervisor: Prof. Dr. Anna Nelles

Abstract

The successful radio-triggered detection of cosmic air-showers with measurements at the Owens Valley Radio Observatory Long Wavelength Array (OVRO-LWA) in 2019 illustrated again the opportunities for cosmic ray detection with radio telescopes. While several background sources such as airplanes, stationary sources close to the array like A/C units of the data processing shelter and nearby cities were identified, rejected by triggers, and removed from the data, a strong source of radio signals at an elevation angle of $15°$ could not be identified so far, as no known emitting objects lie in this direction. An incorrectly reconstructed arrival direction has been excluded. The explanation of the signal and prediction for future measurement runs could increase the detection efficiency of the radio array. In this thesis, the reflection of radio noise, emitted by the nearby city of Bishop, on clouds into the array and alternatively, the deflection of radio noise by a strong atmospheric refractivity gradient were considered as potential causes for the detected background signal. Both possibilities were studied in raytracing simulations, using an atmospheric refractivity model relying on local weather data and cloud data, obtained from the CALIPSO satellite mission. The deflection was excluded as a potential background source due to the unrealistically large atmospheric refractivity gradients required to deflect a ray into the detector at elevation angles above the horizon. It was found that in principle clouds could explain the excess at $15°$. However, to provide proof more dedicated campaigns with additional weather and cloud data for the precise time of measurement are needed.

Contents

1 Introduction

Cosmic messengers are gamma-rays, neutrinos and cosmic rays, that are electrons, protons, and heavier nuclei as well as their antiparticles, flying through space. Their detection on Earth and in space allows studying their sources, astrophysical objects like the Sun, supernovae, and further galactic and extra-galactic objects. However, a majority of the cosmic ray sources are not identified yet, neither the detailed production mechanism and how they are accelerated to energies that exceed the energy reachable by particle accelerators on Earth by far [1].

The flux of cosmic ray decreases with their energy in the form of a powerlaw. Thus the detection of high energy cosmic rays requires large detectors that cannot be situated on satellites or other spacecraft but must be installed on Earth. When high energetic cosmic ray particles enter the atmosphere of the Earth, they interact with the air and create secondary particles, which can themselves interact, creating a particle shower in the air [1]. By detecting this air shower the energy, direction and to some extent also the type of primary particle can be determined [2].

In the last fifteen years, the radio detection of air showers was established, due to the availability of fast digital signal processing units and the study of the effects underlying radio emission in air-showers [3]. Radio cosmic ray experiments were built, for instance, the AERA at the Pierre Augere Observatory or the LOFAR experiment with antenna arrays spread over northern Europe [4, 5]. Both collect data in combination with other air-shower detectors allowing for the particle detectors to trigger the radio array and a cross-calibration of the energy measurement of the used particle detectors. Recently, the OVRO-LWA experiment successfully demonstrated the possibility of self-triggering: the ability to detect air-shower events purely from the signals of the radio array [6]. This technique holds the potential to observe air-showers at very low elevation angles and large distances, where the particles in the shower do not reach the ground, but the radio signal does, as it is only weakly damped in the atmosphere in the very high frequency (VHF) range, where the radio detection takes place. Furthermore, this technique can be applied to antenna arrays, which were built for astronomical purposes without particle detectors at the same location, and thus collect data at low costs. The largest challenge of self-triggering is the sufficient suppression of radio noise. This means to distinguish between anthropogenic radio signals and cosmic ray radio signals.

During the measurement of OVRO-LWA, an excess of radio noise at 15° over the horizon was discovered from certain azimuthal directions [6]. No potential source was found in this direction. In data from AERA, a similar signal at elevation angles significantly over the horizon was visible [4]. One possible explanation is the reflection of radio noise on clouds to the radio array. An alternative explanation could be the deflection of radio signals under non-standard propagation conditions in the atmosphere.

The aim of this thesis is to study if this background signal can be explained by one of the above-mentioned mechanisms by simulating radio propagation under different atmospheric conditions. I will explain the radio signal emission of cosmic ray air-showers, as well as the detection of air-shower radio signals in Chapter 2 together with the OVRO-LWA experiment. In Chapter 3, I will introduce the used radio propagation model, the atmospheric model and how radio signals can be reflected on clouds. Finally, I will present how this model was implemented in a simulation using the software RadioPropa. As input for the simulations, atmospheric data from various sources was required. This data is presented in Chapter 4. The simulation results are presented in Chapter 5. In Chapter 6, I will discuss the results and suggest how experimental data can be used to evaluate the simulation results before concluding.

2 Radio detection of cosmic rays and neutrinos in air

In this chapter, the development of air-showers induced by cosmic rays and neutrinos is described, as well as how radio signals are emitted by the shower through the geomagnetic effect and the Askaryan effect. The detection and the reconstruction of particle properties from the measured shower parameters are explained. The setup and background observations of the cosmic ray radio experiment at the Owens Valley Long Wavelength Array is presented.

2.1 Radio signal emission

When cosmic ray particles enter the Earth's atmosphere, they can interact with air molecules and create secondary particles, which can themselves interact again, producing a cascade of interactions, which is called an air-shower. Air-showers are divided into electromagnetic and hadronic showers, depending on the interaction type of the initial reaction [1]. Electromagnetic showers are mostly initiated by electrons or photons. Highly energetic electrons in matter radiate bremsstrahlung in the form of photons and high-energy photons can produce secondary electrons and positrons by pair production. At the start of a hadronic shower, a nuclear interaction takes place, which produces unstable secondary particles. Among them is a particularly high number of pions, the neutral pion decays into a pair of photons producing an electromagnetic component of the hadronic shower.

At the beginning of an air-shower, the particle number increases due to decays, pair production, and photon radiation. The average energy of the individual particles decreases during this process. When reaching the shower maximum, the point with the most particles in the shower, the energy will not be sufficient to create further particles in pair production and the charged particles no longer emit bremsstrahlung, which causes the cascading to stop. More particles are absorbed by interactions with the air than new particles produced, therefore the total number of particles in the shower decreases.

The electromagnetic component of both shower types emits, besides light, also radio waves, dominantly generated by relativistic electrons and positrons. Two mechanisms for electrons and positrons to emit radio signals were shown to be most important, namely the geomagnetic effect and the Askaryan effect. The geomagnetic effect contributes significantly more in air-showers than the latter effect [2].

The geomagnetic effect is the deflection of charged particles in the Earth's magnetic field due to the Lorentz force. Positrons are deflected in the opposite direction as electrons, leading to a time-dependent transverse current as the particle number in a shower is time-dependent. The time-dependent current emits radiation analogously

to a Hertzian dipole. The resulting radiation is linearly polarized. As electrons and positrons have the highest charge to mass ratio they are deflected the most. Additionally they are abundant in the shower, thus they are the main emitters [2].

The Askaryan effect is caused by a longitudinal charge separation along the shower axis. The shower front accumulates a negative charge excess due to the ionization of air atoms by photons and the annihilation of shower positrons with electrons of air atoms. The charge excess is strongest at the shower axis, where the electron density is highest due to the small angle between the particles created by photon radiation and by pair production processes at highly relativistic energies [1]. The charge of this region is again time-dependent due to the development of the particle number during the shower and consequently produces radio emissions. The emitted radiation is radially polarized analogously to the emission pattern of a time-dependent point charge.

The radio emissions of both effects are coherent at low frequencies as the emitting regions are smaller than the wavelength. Thus the waves of both mechanisms can interfere, leading to an asymmetric radio signal footprint at the ground [2]. The radio signal emitted by the Askaryan effect is radially polarized, the electric field component points towards the shower axis. The electric field component of the radio signal emitted by the geomagnetic effect points in the western direction (for a vertical shower). Therefore the electric field east of the shower core is the constructive interference of both signals and the electric field on the west side is the destructive interference, breaking the radial symmetry [7].

Neutrinos can also be studied in air-shower experiments. As with cosmic rays they can be detected indirectly through the shower triggered by secondary particles created in an interaction of the neutrino with matter [8]. The air-showers triggered by neutrino secondary particles can be distinguished from other cosmic ray air-showers by their starting point deep in the atmosphere due to the low interaction cross-section of neutrinos with the air. Inclined showers are especially suited for looking for neutrinos, as the path through the atmosphere is longer than for vertical showers. A τ-neutrino could also produce an upgoing shower after interacting inside the Earth in a charged-current interaction, creating a τ, which leaves the Earth and decays in the atmosphere [8]. So far, no high energetic neutrinos were detected by air-showers despite thirteen years of observations, giving an upper constraint of the high energetic neutrino flux [9].

2.2 Radio detection of air showers

In classic air-shower experiments, the Cherenkov light of fast-moving charged particles and the fluorescence light of excited nitrogen molecules is detected in the air by telescopes. A different technique is to detect the shower particles reaching the ground, especially electrons and muons, by water-Cherenkov or scintillation detectors [2]. The detection of radio signals of air-showers presents a complementary approach to these techniques. Radio detectors, consisting of arrays of antennas, have a significantly larger duty cycle than photon detectors, which can only work during moonless nights. As the sensitive elements are wire antennas, large areas can be

instrumentalized at low costs. Especially advantageous is the combination of particle detectors with radio arrays to reuse the existing infrastructure for power supply and signal processing, as well as using the particle detector as a trigger for the radio array, which can deliver more precise information about the shower maximum position and energy than the particle detector. A second interesting approach is the parallel use of radio arrays, which were built for astronomical purposes, for astroparticle physics by the technique of self-triggering. The energy threshold of radio detection is about $100\,\mathrm{PeV}$, which makes the technique interesting for the search of the highest energy cosmic ray particles from galactic and extra-galactic origin [2].

The arrival direction of the air-shower is reconstructed by the time differences between the signal detection at individual antennas. The energy of the electromagnetic component of the shower can be calculated from the measured radio energy density at the ground. The energy of the primary particle in a hadronic shower can then be estimated from hadronic interaction models. The distance to the shower maximum can be derived from the size of the radio footprint measured. The determination of the initial particle type is only possible on a statistical basis, comparing simulated signals of particle events with measured signals [5]. The most sensitive shower parameter for this estimation is the position of the shower maximum: the atmospheric depth of the interaction of the primary particle depends on their energy-dependent cross-section, heavier particles interact generally earlier, which results on average in a larger measured distance to the shower maximum.

2.3 The Owens Valley Long Wavelength Array

The Owens Valley Long Wavelength Array (OVRO-LWA) is an antenna array at a radio observatory situated in California, originally built to study galaxy formations, extrasolar planets, and solar radio bursts. It consists of 288 crossed broadband dipole antennas distributed over a $1.5\,\mathrm{km}$ baseline. 251 antennas are arranged in a dense core with a diameter of $200\,\mathrm{m}$. The array is sensitive from $27\,\mathrm{MHz}$ to $85\,\mathrm{MHz}$ [10].

It was recently shown that the array is capable of detecting cosmic ray air-showers using radiofrequency only self-triggering as no particle detectors are situated at this location [6]. As the propagation length of radio signals is longer than the propagation of particles created in the shower, self-triggering holds the potential to detect steeply inclined showers, where the shower maximum is at distances larger than the typical propagation lengths of muons and electrons.

The greatest challenge for applying self-triggering is to distinguish Radio Frequency Interference (RFI) caused by humans from the radio signal of air-shower events. Due to the location of the OVRO, shielded from mountains at two sides from major cities, the radio noise level is rather low. The most prominent sources of noise are the small town Bishop, in a distance of $17.6\,\mathrm{km}$, power lines, airplanes and the electrical infrastructure of the array itself. In the analysis, sources very close to the array ($< 1\,\mathrm{km}$) are rejected, which removes any noise stemming from the array infrastructure, such as the signal processing shelter. Signals with low elevation angles ($< 2°$) and signals from a few azimuthal directions, where a stationary noise

source was found are rejected as well. Airplanes are filtered by their continuous track over time. This lead to successful discrimination of RFI and the detection of cosmic ray air-showers.

During the measurements, an excess of RFI was detected at an elevation angle of $15°$, see Figure 2.1. No geographical feature in the surrounding could be found at this angle, but for the same azimuthal angle sources on the ground were identified. A similar signal was also observed in measurements of the Auger Engineering Radio Array (AERA) in Argentina, see Figure 2.2. At narrow azimuthal directions, an excess of signal was detected over elevation angles up to $30°$. The azimuthal directions were found to coincide with power lines and transformers at the ground.

The detection efficiency of the radio array is given by the ratio of detected cosmic ray events over the number of occurring cosmic ray events. The number of detected events is limited by the successful discrimination of events and RFI. The applied cuts, excluding regions of high RFI noise, necessary to reduce the triggering on background events, thus reduce the detection efficiency. In the OVRO-LWA cosmic ray detection, azimuthal arrival directions from $97°$ out of $360°$ are completely excluded. To increase the detection efficiency by reducing the excluded arrival directions, the observed radio signals have to be explained and a possibility to predict them for the time of the measurement has to be found.

For this aim, the propagation of radio signals in the atmosphere has to be studied and implemented into a simulation to investigate how and under which conditions radio signals emitted in Bishop could reach the radio array besides direct line-of-sight propagation.

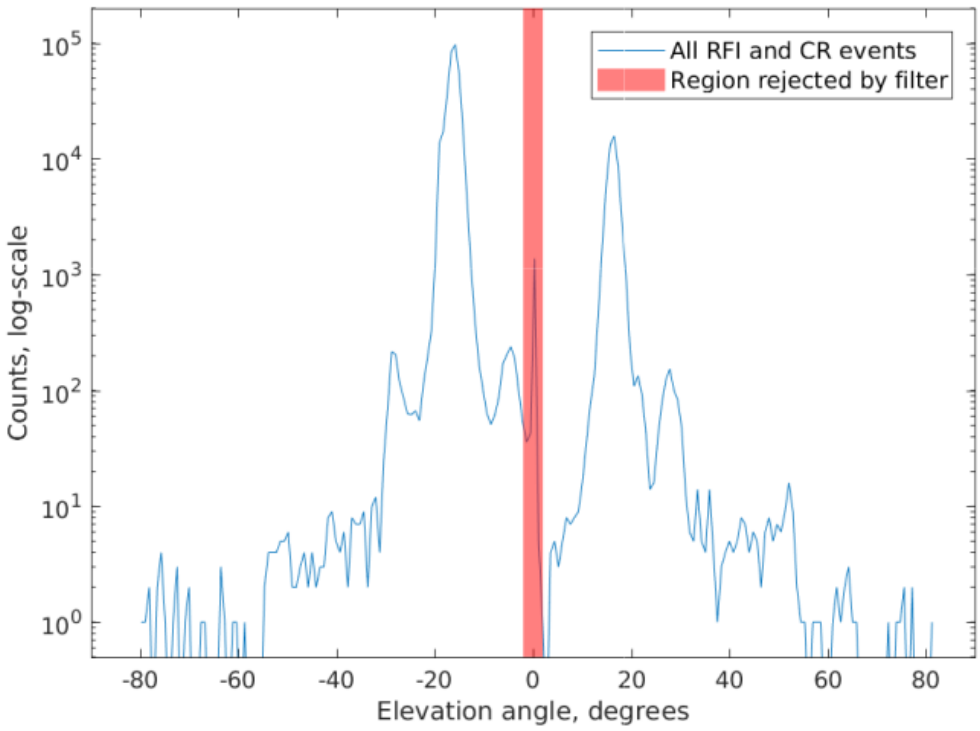

Fig. 2.1: Histogram of elevation angles during a 40 hour measurement at the OVRO-LWA conducted in January 2018. Figure from [6].

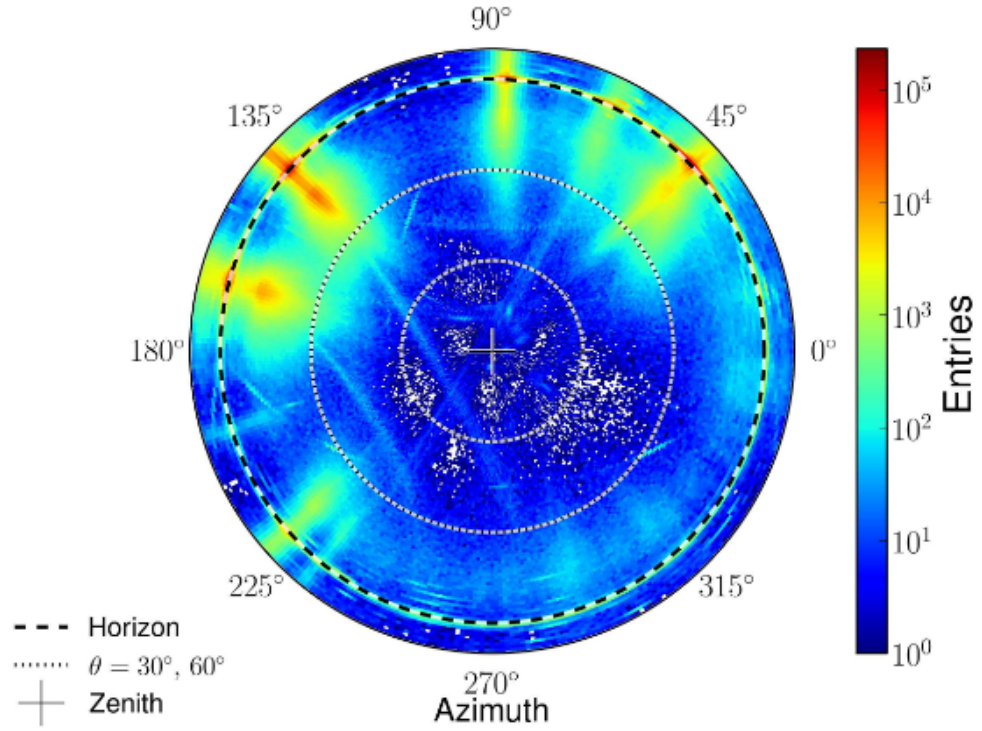

Fig. 2.2: Angular distribution of reconstructed signal directions from AERA measurements from September 2010 to May 2011. Figure from [4].

3 Simulations of radio propagation in the atmosphere

In this chapter, the model and assumptions used to simulate the propagation of radio signals in the atmosphere between the city of Bishop as the source and the OVRO-LWA experiment as the detector are established. The electromagnetic waves of the radio signal are approximated by rays, which paths are determined by the refractive index and refractive index gradient of the propagation medium. For propagation in the atmosphere, the refractive index is expressed by the atmospheric refractivity. An atmospheric model is introduced, which allows calculating the atmospheric refractivity at variable heights dependent on the ground temperature, pressure, and humidity. A simple model for clouds in the atmosphere is described, as well as how the radio signal is reflected on clouds. Finally, the implementation of the presented model in the raytracer simulation software RadioPropa is described.

3.1 Model for radio ray propagation

In the ray model of electromagnetic waves the path of a ray $\mathbf{r}(s)$ parameterized by s is given by the eikonal equation

$$\frac{d}{ds}\left(n(\mathbf{r})\frac{d\mathbf{r}}{ds}\right) = \nabla n \quad , \tag{3.1}$$

where $n(\mathbf{r})$ is the refractive index of the material at the position of the ray. Using a paraxial approximation for the ray, assuming only small changes of the refractive index along the path for individual steps, the approximation

$$\frac{dn(\mathbf{r})}{ds}\frac{d\mathbf{r}}{ds} \approx 0 \tag{3.2}$$

can be used [11]. This simplifies the eikonal equation to

$$n(\mathbf{r})\frac{d^2\mathbf{r}}{ds^2} = \nabla n \quad . \tag{3.3}$$

For radio propagation in the atmosphere, it is assumed that the refractive index changes only with height, but not when moving along a path parallel to the surface of the Earth due to the stratified structure of the atmosphere [12]. Together with the

convention that the curvature radius ρ of the ray is positive when the ray is bending towards the Earth's surface [13], this results in

$$\frac{1}{\rho} = -\frac{1}{n}\frac{dn}{dh} \quad . \tag{3.4}$$

As the refractive index of the atmosphere is close to one and changes only slightly over large distances, the radio refractivity N is used to describe changes in the atmosphere [14]

$$N = (n-1) \cdot 10^6 \quad . \tag{3.5}$$

For near horizontal radio propagation in the atmosphere different propagation scenarios can occure, depending on the radio refractivity gradient dN/dh [12]. Positive gradients lead to *sub-refractivity*, during which the ray bends away from the Earth. For $0 > dN/dh > -79\,\mathrm{km}^{-1}$ *normal refractivity* occurs, where the ray is curved towards the Earth, but with a curvature smaller than the curvature of the Earth's surface, thus gaining height above the Earth's surface with propagation time. During normal refraction conditions, the ray propagates approximately straight. When the gradient lies in the range $-79 > dN/dh > -157\,\mathrm{km}^{-1}$, *super-refractivity* occurs. The beam bents as for normal propagation conditions towards Earth with a curvature smaller than Earth's curvature, but the curvature is no longer negligible. The ray travels approximately parallel to the surface of the Earth for some time, which enables beyond line-of-sight communication. For $dN/dh = -157\,\mathrm{km}^{-1}$ a ray propagates parallel to the Earth's surface. For even lower gradients, the *trapping* condition occurs, describing that the curvature is larger than the Earth's curvature and the ray returns to Earth. Due to repeated reflections on the Earth and the propagation in an arc back to Earth, the ray can travel over long distances close to the Earth. If the trapping is caused by a layer of air with a larger derivative of N below a layer with a smaller derivative of N, this process is called ducting. The ray is trapped between the Earth and the boundary of this lower layer and the propagation resembles the propagation in a waveguide [12]. The different propagation scenarios are depicted in Figure 3.1.

3.2 Atmospheric refractive index model

To calculate the radio propagation in the atmosphere, the radio refractivity and its gradient have to be known at every point. The radio refractivity of the atmosphere depends on the local pressure, temperature, and humidity and can be calculated by the empirical formula [14]:

$$N = 77.6\,\mathrm{K\,hPa}^{-1}\frac{P}{T} - 5.6\,\mathrm{K\,hPa}^{-1}\frac{e}{T} + 3.75 \cdot 10^5\,\mathrm{K}^2\,\mathrm{hPa}^{-1}\frac{e}{T^2} \quad , \tag{3.6}$$

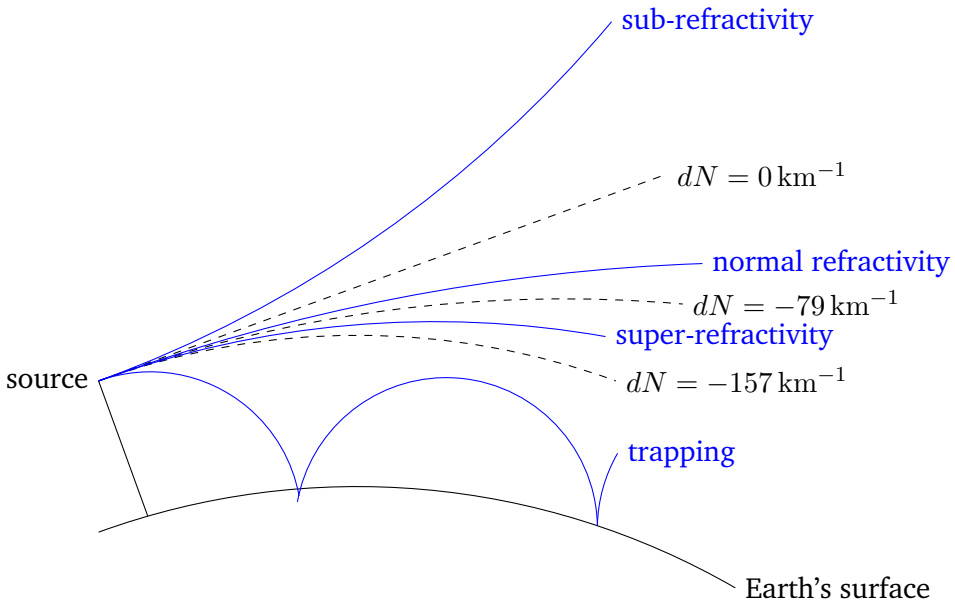

Fig. 3.1: Propagation conditions of radio rays for different values of the radio refractivity gradient. Sketch after [12].

with T being the temperature in K. P is the total atmospheric pressure given in hPa, which is the sum of the dry atmospheric pressure and the water vapor pressure e. The water vapor pressure e can be calculated from the relative humidity H and the saturation vapor pressure for water e_s [14]

$$e = \frac{H}{100} e_s \quad . \tag{3.7}$$

The relative humidity is part of usual meteorological observations, given in percentage %. For the calculation of the saturation vapor pressure of water depending on the temperature and pressure, the Arden Buck equation [15] with the latest values of the coefficients a, b, c and d [14] can be used:

$$e_s = E_{\text{water}} \cdot a \cdot \exp\left(\frac{\left(b - \frac{\vartheta}{d}\right)\vartheta}{\vartheta + c}\right) \tag{3.8}$$

$$\begin{aligned} a &= 6.1121\,\mathrm{hPa} \\ b &= 18.678 \\ c &= 257.14\,^{\circ}\mathrm{C} \\ d &= 234.5\,^{\circ}\mathrm{C} \end{aligned}$$

The temperature ϑ is given in °C. The enhancement factor E_{water} is a correction factor taking into account that the saturated vapor pressure of water in the air is

higher than the saturated vapor pressure of pure water vapor due to molecular interactions. The factor can be calculated according to

$$E_{\text{water}} = 1 + 10^{-4} \cdot \left(7.2 + P\left(0.0320\,\text{hPa}^{-1} + 5.9 \cdot 10^{-6}\,\text{hPa}^{-1}\,^{\circ}\text{C}^{-2}\vartheta^2\right)\right) \quad . \tag{3.9}$$

The enhancement factor is usually close to one and exactly one for an ideal gas system. Using the Arden Buck equation leads to very small deviations from measured values for temperatures interesting for metereological applications ($35\,^{\circ}\text{C}$ to $0\,^{\circ}\text{C}$) [16].

To model the atmospheric refractivity in the area between Bishop and the OVRO-LWA experiment, it is assumed that the refractivity is constant in the horizontal direction. It is assumed that the temperature decreases linearly with height with a fixed lapse rate $L = 6.5\,^{\circ}\text{C}\,\text{km}^{-1}$ starting from the ground temperature T_0

$$T(h) = T_0 - Lh \quad . \tag{3.10}$$

This temperature model is valid for the troposphere, the lowest atmospheric layer [17]. The pressure decreases with height according to the barometric height equation [18]:

$$\frac{dP}{dh} = -\frac{Mg}{RT}P \tag{3.11}$$

with M the molar mass of air, g the gravitational acceleration and R the universal gas constant.

Combined with equation 3.10 and integrated this leads to

$$P(h) = P_0\left(\frac{T_0 - Lh}{T_0}\right)^{\frac{gM}{LR}} \quad , \tag{3.12}$$

where P_0 is the pressure measured at the ground.

The gradient of the refractivity is calculated as

$$\begin{aligned}\frac{dN}{dh} =& 77.6\,\text{K}\,\text{hPa}^{-1}\left(\frac{1}{T}\frac{dP}{dh} - \frac{P}{T^2}\frac{dT}{dh}\right) - 5.6\,\text{K}\,\text{hPa}^{-1}\left(\frac{1}{T}\frac{H}{100}\frac{de_s}{dh} - \frac{e}{T^2}\frac{dT}{dh}\right) \\ &+ 3.75 \cdot 10^5\,\text{K}^2\,\text{hPa}^{-1}\left(\frac{1}{T^2}\frac{H}{100}\frac{de_s}{dh} - \frac{2e}{T^3}\frac{dT}{dh}\right)\end{aligned} \tag{3.13}$$

with the differentials

$$\frac{dT}{dh} = -L \tag{3.14}$$

$$\frac{dP}{dh} = -\frac{P(h)}{T(h)}\frac{Mg}{R} \tag{3.15}$$

$$\frac{de_s}{dh} = -e_s(h)\frac{\vartheta}{\vartheta + c}\left(\frac{b}{\vartheta} - \frac{2}{d} + \frac{b}{\vartheta + c} - \frac{\vartheta}{d\,(\vartheta + c)}\right)L \tag{3.16}$$

The relative humidity is assumed to be constant with height. The enhancement factor E_{water} is not derivated as its gradient is of the order of magnitude of 10^{-7} for usual conditions.

With this set of equations the radio refractivity and the radio refractivity gradient can be calculated, with the ground temperature T_0, total air pressure on the ground P_0 and relative humidity on the ground H as only free parameters.

3.3 Radio reflections on clouds

Clouds are modeled for the simulations of this thesis as sections in the atmosphere with a relative humidity of 100%. This leads to a sudden change in the radio refractivity. At the boundary layer between areas with different refractive indices, the radio waves are partially reflected. The intensity fraction of the reflected ray is described by the Fresnels equations dependent on the incidence angle of the ray θ [19]:

$$R_s = \left| \frac{n_{\text{air}}\cos\theta - n_{\text{cloud}}\sqrt{1 - \left(\frac{n_{\text{air}}}{n_{\text{cloud}}}\sin\theta\right)^2}}{n_{\text{air}}\cos\theta + n_{\text{cloud}}\sqrt{1 - \left(\frac{n_{\text{air}}}{n_{\text{cloud}}}\sin\theta\right)^2}} \right|^2 \tag{3.17}$$

$$R_p = \left| \frac{n_{\text{air}}\sqrt{1 - \left(\frac{n_{\text{air}}}{n_{\text{cloud}}}\sin\theta\right)^2} - n_{\text{cloud}}\cos\theta}{n_{\text{air}}\sqrt{1 - \left(\frac{n_{\text{air}}}{n_{\text{cloud}}}\sin\theta\right)^2} + n_{\text{cloud}}\cos\theta} \right|^2 \tag{3.18}$$

$$R_{\text{eff}} = \frac{1}{2}\left(R_s + R_p\right) \tag{3.19}$$

R_s gives the reflectivity for s-polarized waves, R_p for p-polarized waves. Both polarizations can be detected by the array. The polarization of the source is unknown, it was assumed that the signal is unpolarized. The effective reflectivity R_{eff} is used to account for equal power in the s- and p-polarization of the unpolarized signal.

Additionally to the water vapor saturated air, clouds contain water droplets with a typical diameter of $8\,\mu\text{m}$ for continental clouds and $14\,\mu\text{m}$ for maritime clouds [20]. In atmospheric regions with temperatures below $0\,^\circ\text{C}$ ice crystals can be present,

which have irregular shapes and a very broad diameter distribution from $2\,\mu\mathrm{m}$ to $10\,\mathrm{mm}$ depending on the temperature of the cloud, but with a majority of the crystals below $200\,\mu\mathrm{m}$ [21]. Rayleigh scattering on the water droplets and ice crystals is not considered in this thesis, as the wavelength of the used radio frequencies in the OVRO-LWA experiment is with $3.5\,\mathrm{m}$ to $11.1\,\mathrm{m}$ several orders of magnitude larger than the diameter of the particles in the cloud and the scattered intensity on spherical particle scales according to [22]

$$I \propto I_0 \frac{d^6}{\lambda^4} \quad , \tag{3.20}$$

where d is the diameter of the spherical droplets and λ the wavelength of the incident radiation. Additionally, the Rayleigh scattering is non-directional and as such, even if it is contributing, cannot explain the distinct arrival directions of the background.

Also, Bragg diffraction, the constructive interference of light scattered on a regular particle grid, is not considered here as the occurrence condition is, that the wavelength is of comparable size to the particle spacing and the wavelength is significantly larger than the distance between the droplets or ice crystals in the cloud [23].

3.4 RadioPropa simulation software

For the simulation of the radio propagation in the atmosphere, the software RadioPropa was used [11]. In this modular raytracer, the eikonal equation (equation 3.1) is solved in the paraxial approximation (equation 3.3) for propagation inside materials with continuous refractive index gradient by the Cash-Karp method. For a transition between different media or an abrupt change in refractive index, the direction of reflected and transmitted rays are calculated according to Snell's law and the amplitude of both rays is calculated according to Fresnel's equations.

The raytracer is implemented in C++ and can be compiled into a python library, where the simulation is set up and the resulting data processed. The existing code was enhanced and extended with the following features to allow the simulation of the scenarios considered in this thesis: [1]

- The atmospheric refractivity model, as described above, was implemented as a class *CloudModel* inheriting from the class *ScalarField* into the C++ code. By implementing equation 3.6 the radio refractivity can be calculated and the definition of N (equation 3.5) is used to calculate the refractive index. Equation 3.13 is implemented to calculate the refractivity gradient at every step of the simulation, from this value the refractive index gradient is calculated. The weather conditions at the ground (ground temperature T_0, ground pressure P_0 and humidity H), as well as the height of the lower and upper cloud boundary, are provided to the constructor of the class. For the calculation of the refractive index and refractive index gradient values, it is distinguished between a point

[1] The code including the atmospheric model is available at: https://github.com/nu-radio/RadioPropa

in the clear atmosphere using the humidity value provided and a point inside the clouds, setting the humidity to 100%.

- The *Observer* class was modified to write for every detection of a ray at a specified region of the detector the elevation angle, intensity and propagation time of the incoming angle into a file. The intensity of the ray, calculated from the square of the absolute value of the vector-valued amplitude, is divided by the square of the propagation length of the ray to account for the intensity decline of a spherical monochromatic wave [24]. The parameters of the atmosphere and the elevation angle of the ray at the source are written in the same file as the ray parameters on detection by the python script that sets up the simulation.

The simulation is set up in the python script by first initializing the atmosphere as the propagation medium with the given weather conditions. Then boundaries are added at every transition from the regular atmosphere to clouds. The refractive indices at the two sides of the layers are calculated by the *getValue* method of the *CloudModel* class at heights $0.1\,\mathrm{m}$ above and below the desired cloud height. The detector is modeled by the surface of a sphere with a radius of $100\,\mathrm{m}$ as the dense core of the OVRO-LWA possesses the same radius [6]. The detector is placed at a distance of $17.6\,\mathrm{km}$ to the source representing the distance between the city center of Bishop and the center of the OVRO-LWA [25]. For the simulation of deflection in the atmosphere without clouds, it was also considered, that the detector is located $65\,\mathrm{m}$ lower than Bishop [25]. An additional height deviation from a straight line between Bishop and the detector is introduced by the curvature of the Earth, resulting in $24\,\mathrm{m}$ on $17.6\,\mathrm{km}$. A flat detector was used in this scenario to read out the elevation angle of the incident rays more precisely. The source of the rays is placed at the origin of the coordinate system and emitting rays into the positive x-z-plane at elevation angles defined in a parameter array. To accelerate the simulations, left of the source, right of the detector, below the Earth's surface and well above the cloud layers detection planes are introduced, which do not record rays, but deactivate them on detection to avoid the full simulation of rays until reaching the set maximal propagation length out of the region of interest. The propagation of the rays is then calculated using the modular ray tracer. In the continuous medium the minimal propagation step is set to $1\,\mathrm{m}$, the maximal step size is $10\,\mathrm{m}$, and the error estimate tolerance is set to $1 \times 10^{-4}\,\mathrm{m}$. The full trajectory of all simulated rays is written to a separate file.

If only the intensity of the reflected ray, but not the exact trajectory is important and normal propagation conditions are prevailing, the ray can be assumed as straight, and only a single ray was simulated. The ray was emitted at the source with the elevation angle

$$\alpha = \arctan\left(\frac{h_{\text{clouds}}}{d/2}\right) \quad , \tag{3.21}$$

where h_{clouds} is the height of the bottom of the cloud layer and d the distance between detector and source. The standard cloud height was $2\,\mathrm{km}$ and the distance between detector and source $17.6\,\mathrm{km}$. The geometry of the simulation setup for a single straight ray can be seen in Figure 3.2.

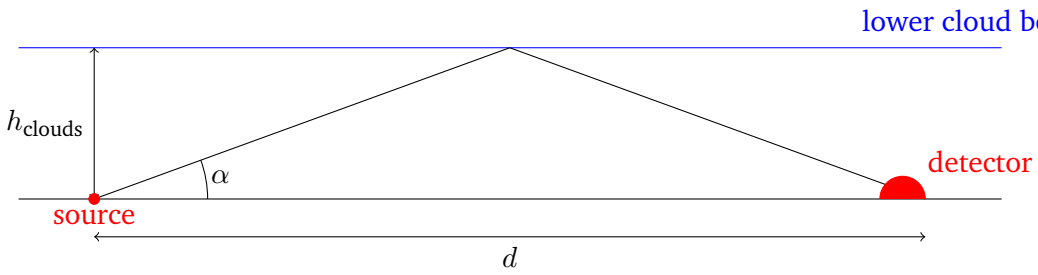

Fig. 3.2: Geometry of the simulation setup for a single cloud layer.

To study with the presented model, implemented into a raytracing simulation, the background signal reaching the detector for given time intervals or situations, weather and cloud data for this period are required.

4 Atmospheric data

The atmospheric data used for the simulations is presented in this chapter. At first, the assumptions for the height dependence of temperature, pressure, and humidity made for the atmospheric refractivity model should be tested. To evaluate the validity of these assumptions, the used theoretical models were compared to measured vertical profiles. To analyze the atmospheric conditions for a given point in time, the temperature, pressure and humidity values measured at the ground have to be known. This data can be obtained from a weather station in Bishop. The structure of the data and an analysis of the weather data during the days of the measurements at OVRO-LWA is presented. Further data is required to model the clouds, most importantly the cloud height. Cloud data can be accessed from the CALIPSO satellite mission. A description of the data set and an analysis of the cloud conditions for January 2018 and July 2018 is provided.

4.1 Vertical Profiles

To test the validity of the assumptions of the temperature, pressure, and humidity profiles and thus the refractivity calculated from these values, the model predictions of the atmosphere were compared with measured atmospherical vertical profiles. Monthly averages of vertical profiles of temperature, pressure, and humidity are provided by the International Telecommunication Union (ITU) for 353 locations worldwide based on 10 years (1980 - 1989) of radiosonde observations excluding data recorded during rain [17]. The profile data is given in steps of $500\,\mathrm{m}$ up to a height of $16\,\mathrm{km}$, recorded at 00.00 UTC and 12.00 UTC.

The stations closest to Bishop are San Diego, California, Tucson, Arizona, Salt Lake City, Utah and Medford, Oregon. Bishop lies in the Owens Valley between the Inyo and Sierra mountains at an elevation of $1260\,\mathrm{m}$. The climate is classified as a cold desert climate (arid) in the Köppen climate classification [26]. San Diego is closest to Bishop with a distance of $525\,\mathrm{km}$ but has a hot-summer mediterranean climate [26]. During the summer a marine layer occurs leading to unusual temperature and pressure profiles [27]. Medford has a distance of $673\,\mathrm{km}$ and also has a mediterreanean climate [26]. Salt Lake City lies on a similar height as Bishop with $1288\,\mathrm{m}$ elevation and has a distance of $677\,\mathrm{km}$ to Bishop. The climate is classified as mediterranean-influenced hot-summer humid continental climate [26]. Tucson lays at a distance of Bishop of $885\,\mathrm{km}$ and a height of $728\,\mathrm{m}$, the climate is hot semi-arid, which is in the same climate main group as the cold desert climate in Bishop. Thus, as a station for the vertical profile data, Tucson was chosen here.

The temperature, pressure, and humidity values of the data sets are plotted over height for January (Figure 4.1) and July (Figure 4.2). The model predictions were calculated from the lowest available measurement point. In January a fairly good

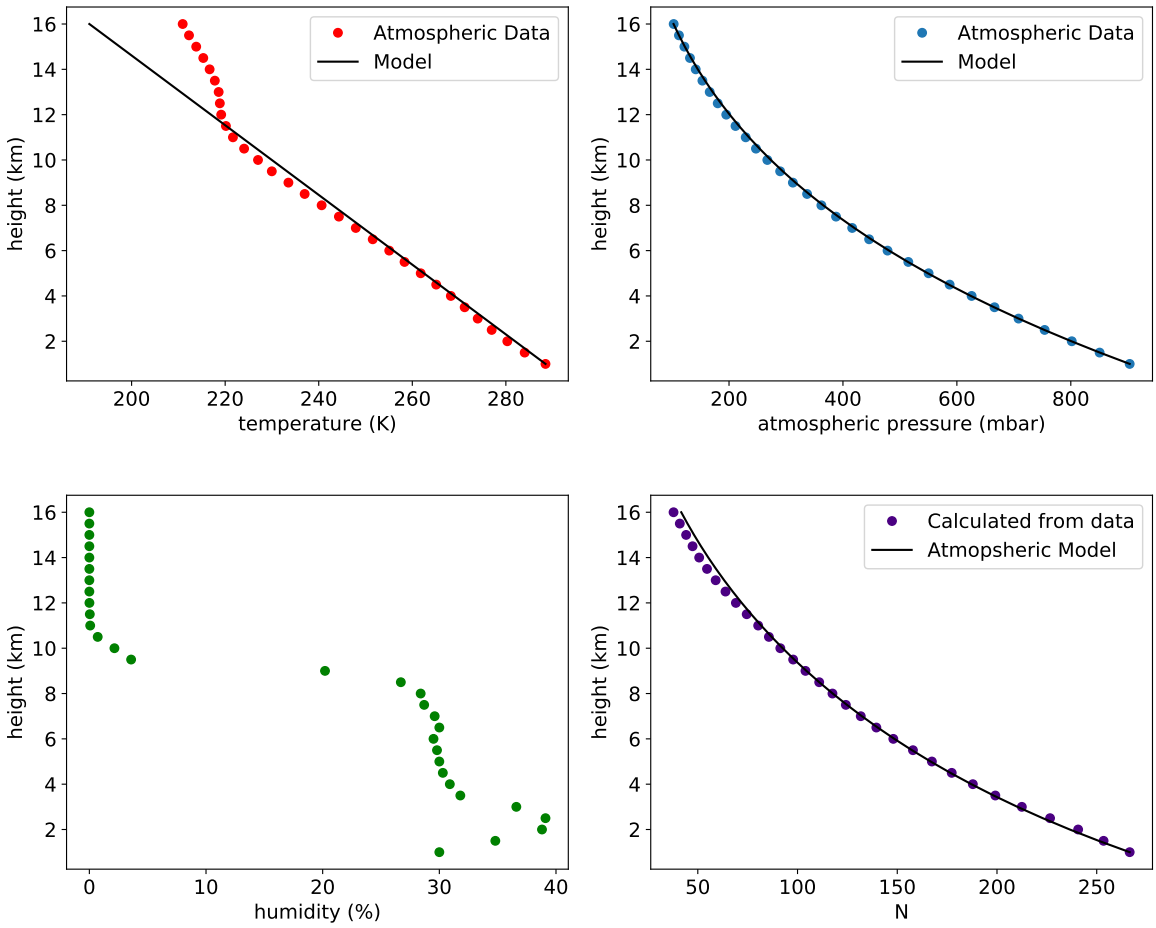

Fig. 4.1: Comparison of monthly averaged vertical atmospheric profiles for January in Tucson, Arizona, at 00.00 UTC, corresponding to 17.00 local time, with predictions of the atmospheric profiles based on temperature, humidity and pressure on the surface. Atmospheric data from ITU [17] [28].

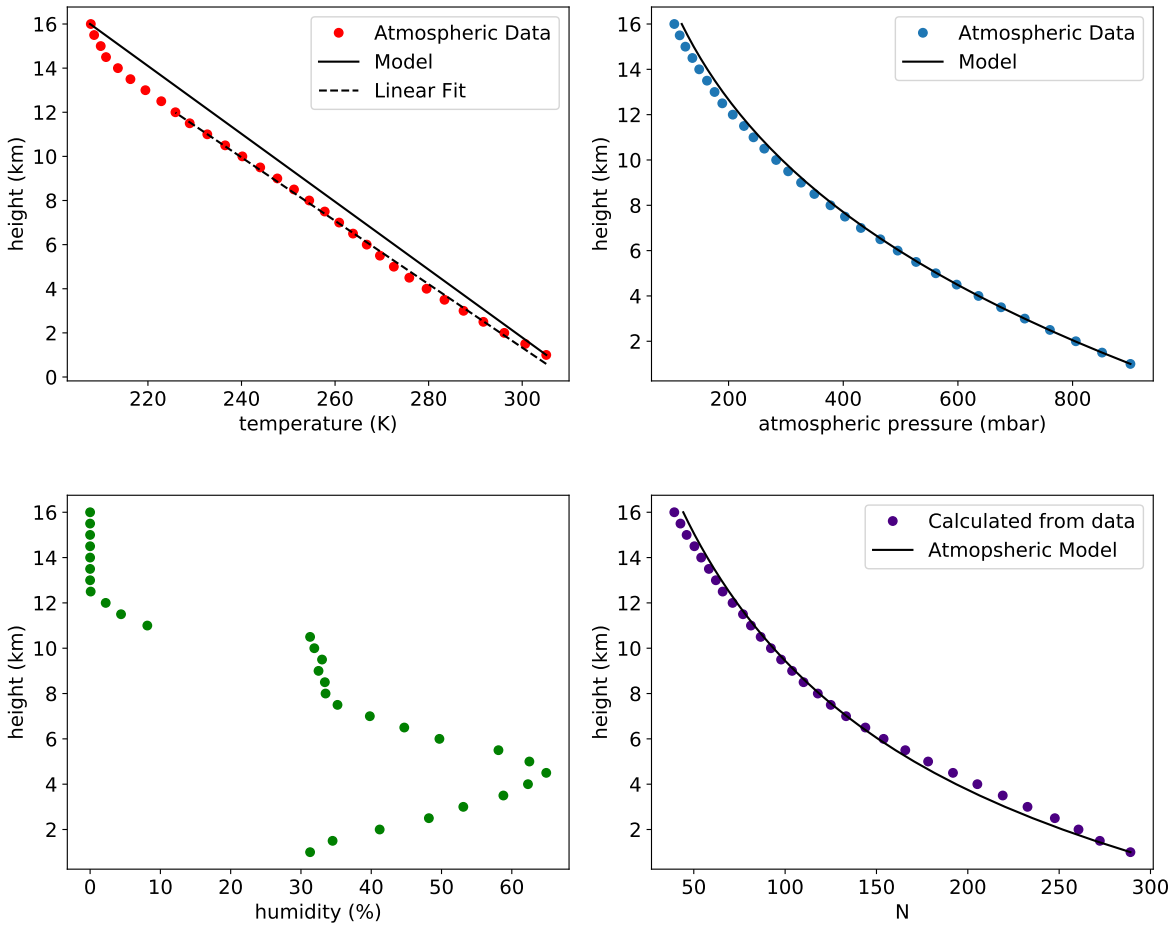

Fig. 4.2: Comparison of monthly averaged vertical atmospheric profiles for July in Tucson, Arizona, at 00.00 UTC, corresponding to 17.00 local time, with predictions of the atmospheric profiles based on temperature, humidity and pressure on the surface. Atmospheric data from ITU [17] [28].

agreement between the model temperature and the measured temperature exists at lower heights. At about $11\,\mathrm{km}$ height the tropopause, the end of the troposphere, can be observed in a change of the temperature lapse rate [29]. The measured pressure values are precisely predicted by the model. Contrary to the assumption, the measured relative humidity changes over a wide range. The humidity shows a complex behavior with height and drops to 0% at the tropopause. The confinement of water vapor to the troposphere is observed globally [29]. For the model, a constant humidity is assumed and the humidity value measured at the ground is taken. Despite large deviations of the relative humidity value, this leads to rather small deviations between the refractivity calculated from data and model refractivity. This is due to two reasons: In equation 3.6 the dry air term is usually dominating as the water vapor pressure in the atmosphere is about three orders of magnitude smaller than the total atmospheric pressure, and the saturation vapor pressure is decreasing approximately exponentially with height as the temperature is decreasing linearly. Thus the largest deviations at large altitudes do not contribute significantly. Overall, the resulting refractivity calculated from temperature, pressure and humidity profiles shows a good agreement with the model, especially below $10\,\mathrm{km}$, which was the region of interest for this thesis.

In July a deviation from the tropospheric temperature lapse rate can be observed. The actual lapse rate was determined with a linear fit with data points up to $12\,\mathrm{km}$ as $L = 7.0\,\mathrm{km}^{-1}$. An increased temperature lapse rate in summer is observed in several other mountainous regions [30]. In general, the tropopause is higher over hot regions, thus it is higher in the summer for mid-latitude regions of the Earth [29]. The pressure prediction agrees for lower altitudes precisely with the measured profile but shows a deviation for large altitudes. This deviation cannot be purely explained by an increased temperature lapse rate, as the model prediction for the temperature-dependent pressure using the temperature lapse rate determined via a linear fit, still shows a deviation from the data points. The humidity varies over a greater range than in the winter and also decreases to 0% at the tropopause. The resulting calculated refractivity shows larger deviations between prediction and measured data than in January. The deviations at high altitudes stem from the deviation between model and data for the pressure, but this altitude region is not of interest for this study. The deviation at lower altitudes cannot be easily explained. When using the corrected temperature lapse rate for the refractivity prediction, the model and data points do not have a significantly better agreement. The relative humidity has a larger influence on the refractivity in summer than in winter due to a higher value of the temperature-dependent water vapor saturation pressure. A height dependent humidity model could resolve the deviation of the model from the recorded data, but no suitable model was found.

The calculations were repeated for the three other stations closest to Bishop, see Figure 4.3. Overall a good agreement between the model and the data is found, especially for lower altitudes and in winter. The non-monotonous behavior at low altitudes in the refractivity of San Diego in summer is due to a temperature inversion and high humidity at the ground, both are explained by the phenomenon of the marine layer.

It can be concluded that, especially in winter, a very precise prediction of the atmospheric refractivity profile of the troposphere, up to heights of $10\,\mathrm{km}$, based on

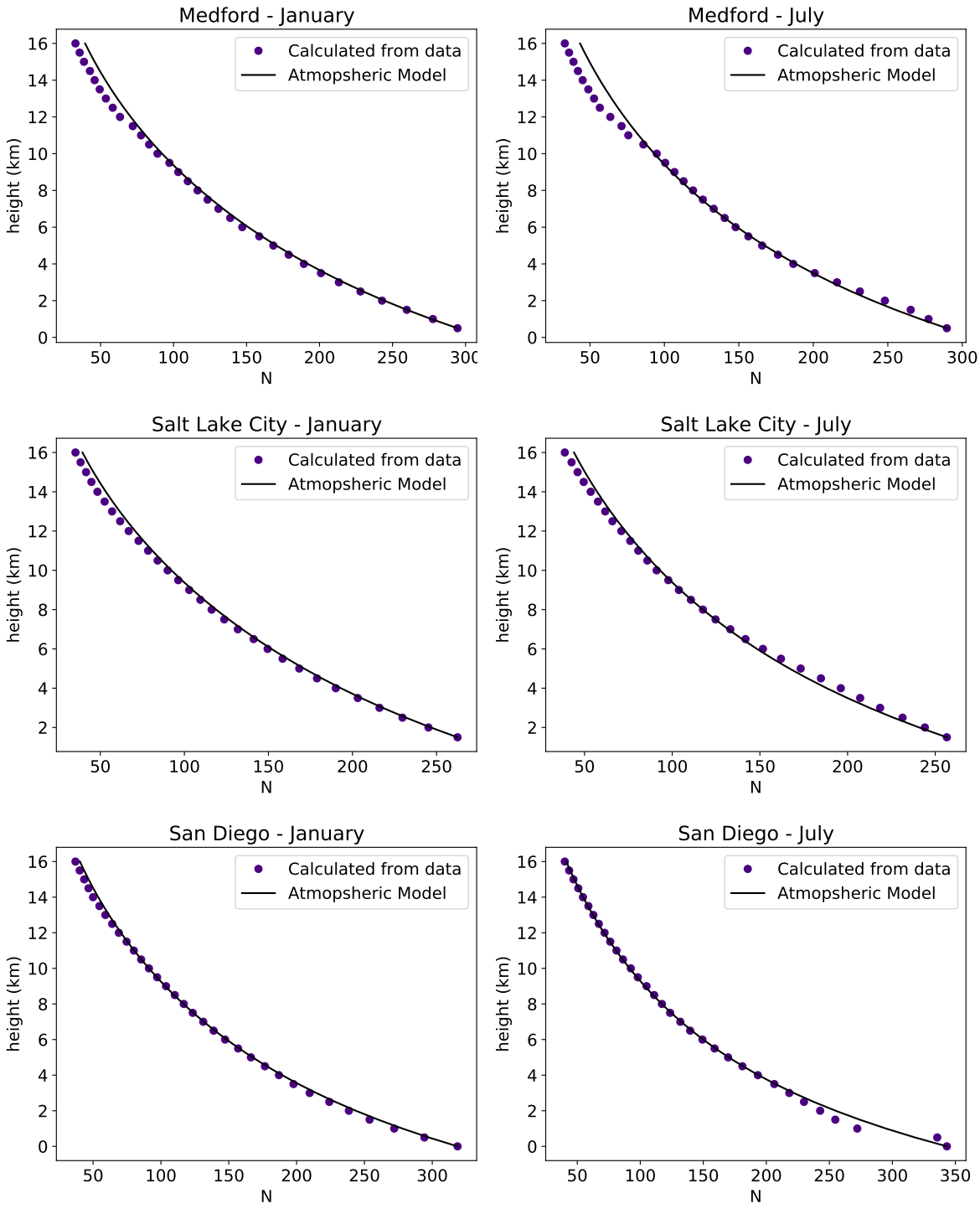

Fig. 4.3: Predictions of the atmospheric refractivity calculated from temperature, pressure and humidity at the ground and refractivity calculated from measured vertical profiles in January and July for three different locations around Bishop.

temperature, pressure, and humidity at the ground is possible. This agreement was found for four different climate types for stations surrounding the area of Bishop and therefore, despite the different climate classification, this conclusion can be transferred to the climate of Bishop, where no profiles are available. Thus, our model assumptions are a good first step to evaluate the feasibility of radio reflections in the atmosphere, provided local weather data is available.

4.2 Local weather data

For the prediction of the refractivity, required to simulate the radio propagation, the temperature, atmospheric pressure and humidity at the ground have to be known for the time of interest. Local weather data for Bishop is available from the Eastern Sierra Regional Airport in Bishop. The recordings contain hourly measurements of temperature, humidity, wind speed and direction, the pressure and the precipitation volume, as well as a description of the sky or precipitation condition, e.g. 'rain' or 'partly cloudy' [31].

This data was evaluated for the time of the OVRO-LWA measurements, see Figure 4.4. During the three days of measurements, which were cloudy and rainy, large variations in the three observables, that determine the atmospheric refractivity, were recorded. The temperature varied about $15\,\mathrm{K}$, the pressure about $15\,\mathrm{hPa}$ and the humidity between 50% and 100%. This leads to calculated refractivity values, between 267 and 289. The large changes in the weather conditions are expected to lead to large changes in the relative strength of the background signal, which will be calculated later. The quick changes of the weather condition point out the necessity of frequent recording of the weather parameters, which is given in this data set.

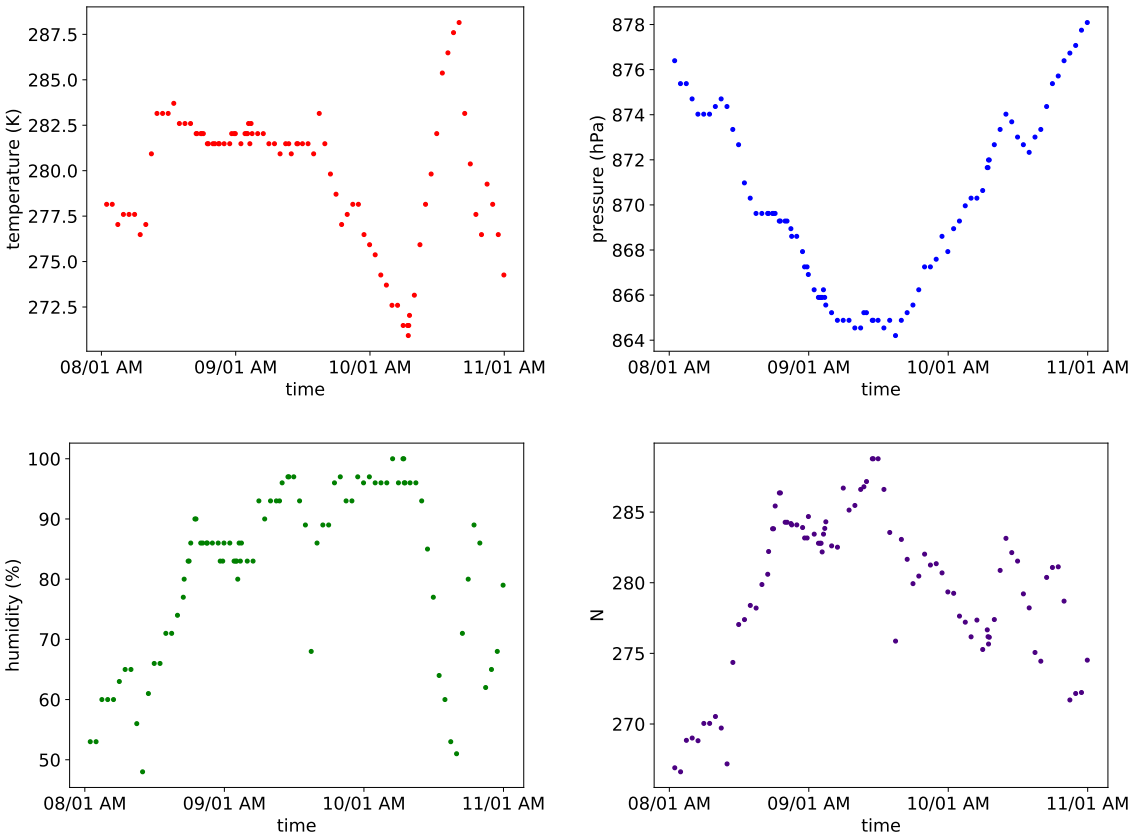

Fig. 4.4: Temperature, pressure and humidity parameters and the calculated atmospheric refractivity at the ground during the measurements at the OVRO-LWA. Weather data was taken at the Eastern Sierra Regional Airport in Bishop and provided by Weather Underground [31].

4.3 Cloud data

The knowledge of the occurrence of clouds and the height of cloud layers are required to determine if and how strong the clouds can reflect radio waves. The occurrence of clouds as sky condition is part of usual weather recordings. In weather recordings by the US National Weather Service the sky conditions are classified according to the percentage of the sky, that is covered by opaque clouds: $5\,\%$ or less is 'Clear', $6\,\%$ to $25\,\%$ 'Mostly Clear', $26\,\%$ to $60\,\%$ 'Partly Cloudy', $61\,\%$ to $87\,\%$ 'Mostly Cloudy' and $88\,\%$ to $100\,\%$ is 'Cloudy' [32].

The height and thickness of cloud layers are not part of the usual local weather recordings, but global cloud data is gathered via satellite missions. It was found from the CALIPSO mission by lidar measurements (light detection and ranging) that, globally, over land the most frequently occurring cloud top layer height is between 2 and $3\,\mathrm{km}$ [33]. Most clouds over land have a thickness of 250 to $750\,\mathrm{m}$ [33]. The reflection is assumed to take place at the bottom of the cloud. The given numbers indicate that the height of most of the cloud bottom layers is in the region from 1.25 to $2.75\,\mathrm{km}$.

The cloud data from the CALIPSO mission can be accessed for specific locations and times [34]. Since the mission consists of a single satellite, data for a specific location or region is only available at a coarse time resolution as the orbit repeats only every 16 days. The data used in this thesis is recorded at a resolution of $1\,\mathrm{km}$ on the surface of the Earth. The vertical resolution for an altitude between $0.5\,\mathrm{km}$ and $8.2\,\mathrm{km}$ is $30\,\mathrm{m}$, between $8.2\,\mathrm{km}$ and $20.2\,\mathrm{km}$ altitude, the resolution is $60\,\mathrm{m}$ [35]. Data recording of the mission was started in June 2006 and is still running.

For the selected CALIPSO data files, the cloud layer base altitude, measured by lidar, was readout. The surface elevation at the location of the lidar footprint was subtracted to get the cloud height above the surface. Measured cloud base heights smaller than $0.5\,\mathrm{km}$ were excluded from the analysis. All cloud layers were taken into consideration, up to three cloud layers for each point were detected. Clouds were only considered for the analysis if the cloud-aerosol discrimination score was higher than 90, which gives the level of confidence that the detected scattering layer in the atmosphere is indeed a cloud [35].

For the days of the proof-of-principle measurement, there were three overflights over California. From these overflights one measurement point closest to Bishop was chosen, each under the condition that this point was recorded over land. One data point had to be excluded from the analysis, due to a very low detected cloud height. The two available data points allow no detailed insights of the cloud conditions and its development for the time of the measurement, which is required for a precise signal background prediction. Therefore longer time intervals are considered to study the general influence of clouds on the background signal.

The distribution of the altitude of the lower cloud boundaries for January 2018 and July 2018 determined from 7374 and 6692 measurement points from the CALIPSO mission in an area of $500\,\mathrm{km} \times 500\,\mathrm{km}$ around Bishop is shown in Figure 4.5. In January, in $56.7\,\%$ of the measurement points at least one cloud layer was detected,

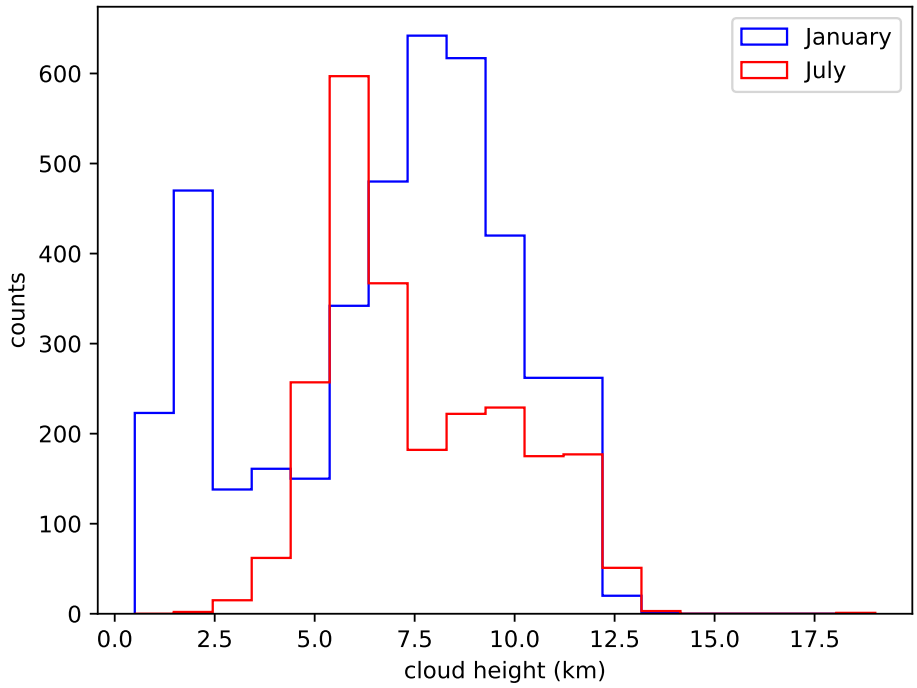

Fig. 4.5: Histogram of measured lower cloud layer boundary altitudes in January 2018 and July 2018 in an area of $500\,\mathrm{km} \times 500\,\mathrm{km}$ around Bishop. Data from [34].

in July only $35.4\,\%$ of the measured points showed a cloud, which indicates that more days without background signal should occur in summer. In January the distribution shows two peaks, one below $2.5\,\mathrm{km}$ and one at $7.5\,\mathrm{km}$. In July no clouds with a lower boundary height below $2\,\mathrm{km}$ were measured. The distribution shows only one peak, it is shifted towards lower heights with respect to the second peak in January. The shown cloud height distribution is used later in the simulations as additional input to the local weather data.

On the general availability of atmospheric data, it can be concluded that very detailed weather recordings for Bishop are available, which allow for a precise prediction of the atmospheric refractivity at the ground. The atmospheric refractivity at larger altitudes is given by the employed atmospheric model. A good general agreement between the model prediction and the atmospheric refractivity predicted from the measured profiles was found, but as the profiles are monthly averages and recorded for a location far from Bishop, no short-lived or local conditions are considered. The cloud data is only available with a sufficient number of data points when a large region and long time interval is considered.

The presented data is used as input for the simulation of radio propagation: the available local weather data allows the precise modeling of the refractivity of the atmosphere at any time, which can be used for the modeling of the conditions during the measurement day. The cloud data can be used in combination with the weather recordings at the time of the cloud data recording for more general predictions, as

the spatial and time resolution of the cloud data is not sufficient for predictions for the measurement day.

5 Simulation results

At first, the influence of the weather parameters temperature, pressure, and humidity on the relative intensity of reflections on clouds was investigated. The dependence of the atmospheric refractivity on these parameters was analyzed, as well as the relative intensity of a ray reaching the detector after a reflection on the cloud. The weather data of January and July 2018 was analyzed to determine how frequently conditions with high reflected intensities occur. In the next step, the cloud data was taken into account: the relative intensity of reflected rays dependent on the cloud height was studied. Histograms of the elevation angle under which the highest background intensity is expected were created. As alternative propagation mechanism of radio noise into the detector the deflection of rays by strong atmospheric gradients was considered. Finally, a prediction of the development of the relative intensity over the course of the measurement days at OVRO-LWA was calculated, using once a fixed cloud height and once a simple model for a changing cloud height.

5.1 Reflections on clouds dependent on weather conditions

The intensity of a ray reflected on a cloud is given by the difference in refractivity between inside and below the cloud. The dependence of the atmospheric refractivity on the local weather parameters can be seen in Figure 5.1. For the parameters that are not varied the annual average value for Bishop is used. The temperature has the largest influence on the refractivity for the parameter ranges shown in the plots. For higher temperatures, the difference between the refractivity below and above the cloud boundary layer is higher as the water saturation pressure is higher and thus the same relative humidity difference results in a larger water vapor pressure difference. The pressure does not influence the refractivity difference, the complete curve is only shifted to lower or higher refractivity values. For lower humidity values of the clear atmosphere, the difference in humidity between inside the cloud and below the cloud is larger and thus the jump in refractivity is also.

The reflection of a single ray on a closed cloud cover of $2\,\mathrm{km}$ height was simulated for different temperature, pressure, and humidity values at the ground while using the annual average values for Bishop if a parameter is kept fixed. When temperature and pressure are varied (Figure 5.2), the pressure is not influencing the reflected amplitude, as expected, since the refractivity difference is not influenced. The reflected amplitude increases when the temperature is increasing. When temperature and humidity are varied (Figure 5.3) for high temperatures and low humidity values the reflected ray has the strongest intensity. The slope of the lines of equal reflected intensity in units of $\%/\mathrm{K}$ tell, which of the two parameters is more significant. At low temperatures the slope is larger than one, this means that an increase in temperature

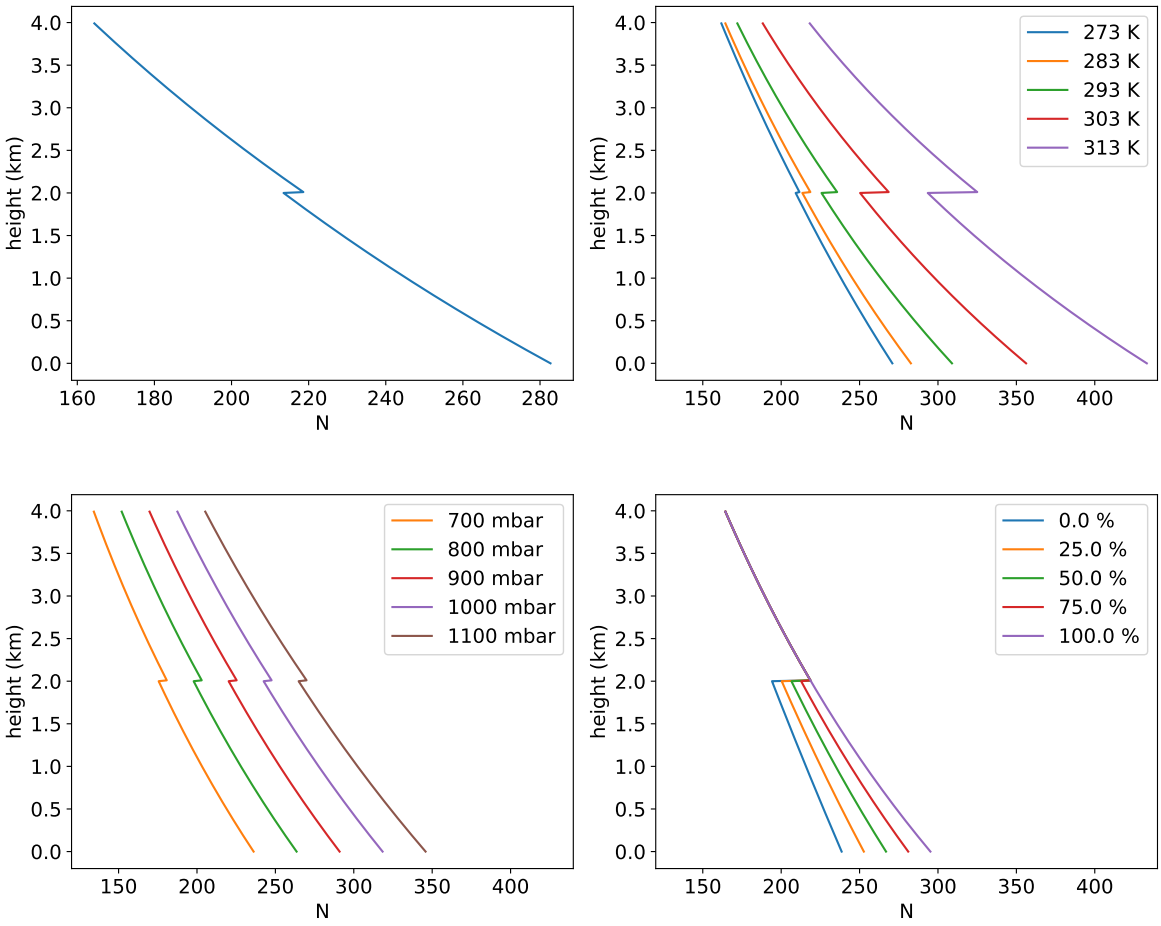

Fig. 5.1: Atmospheric refractivity with cloud layer starting at $2\,\mathrm{km}$ using the annual average values for Bishop (upper left) and dependence on ground temperature (upper right), pressure (lower left), and humidity (lower right).

of $1\,\mathrm{K}$ has a larger influence on the reflected intensity than an increase in humidity of $1\,\%$. The slope is decreasing slightly towards higher temperatures, the humidity has an increasing impact at high temperatures. Towards higher humidity values all the lines are converging towards a single horizontal line. This means that the humidity has a much higher influence on the reflected ray than the temperature. In this region, the reflected intensity approaches zero and therefore the shown logarithm of the relative intensity is diverging. For the simultaneous variation of humidity and air pressure (Figure 5.4), the intensity is again not influenced by the air pressure, but the reflected intensity is higher if the humidity is lower.

It can be concluded that the highest reflected intensities are expected for high temperatures and low humidity values. To study how often these conditions prevail at the location of the OVRO-LWA, the complete set of hourly weather data of January 2018 and July 2018 from the Eastern Sierra Regional Airport was analyzed [31]. The frequency of temperature and humidity values have to be considered together, see Figure 5.5, histograms of only one of the parameters do not allow to study the frequency of certain refractive conditions. The temperature fluctuations in both months were about $30\,\mathrm{K}$ and in both month relative humidity values from $0\,\%$ to

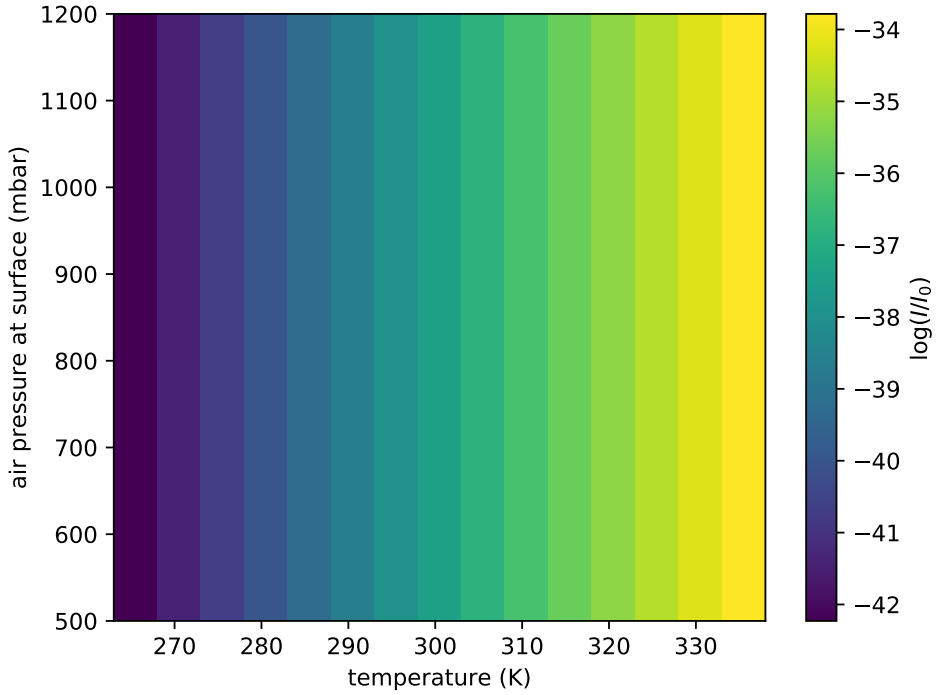

Fig. 5.2: Simulated logarithmic relative intensity of a ray reaching the detector by reflection on a cloud depending on ground pressure and temperature.

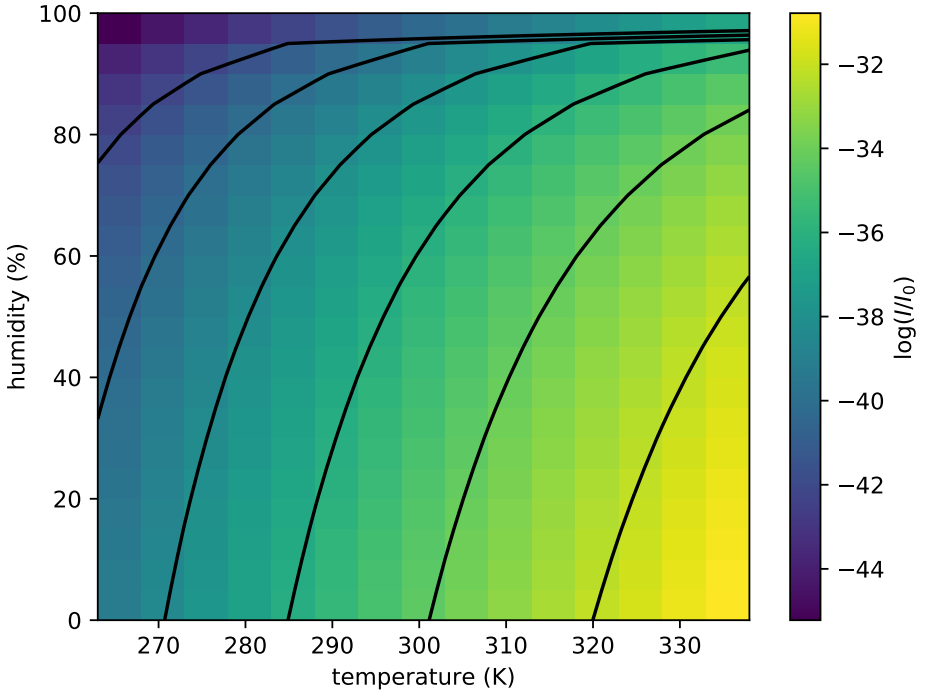

Fig. 5.3: Simulated logarithmic relative intensity of a ray reaching the detector by reflection on a cloud depending on ground temperature and humidity. The lines indicate parameter combinations with an equal simulated intensity value.

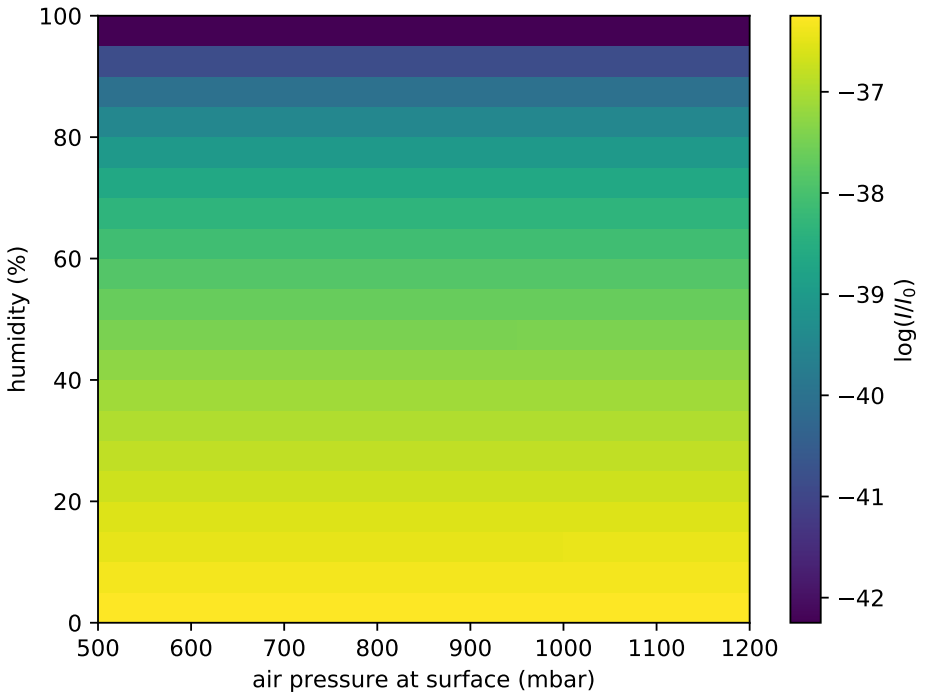

Fig. 5.4: Simulated logarithmic intensity of a ray reaching the detector by reflection on a cloud depending on ground pressure and humidity.

100 % occurred. In July low humidity values are more frequent and the temperature is higher. In January the temperatures are generally lower and high humidity values occur.

The resulting refractivity difference between directly below and above the cloud boundary layer was calculated from the weather data. In the temperature and humidity histograms lines of equal refractivity differences are shown. The weather observations of January are distributed over a larger area, but as temperatures are low, the resulting changes in refractivity difference are small when temperature or humidity is varied. In July the values are concentrated in regions of high refractivity difference, in a region, where temperature and humidity have the strongest impact on the refractivity difference. Additionally, sky observations were taken into consideration. It was distinguished between sky conditions, where the sky is mostly covered (cloudy and mostly cloudy) and where the sky coverage is smaller (partly cloudy) and therefore the probability for rays to be actually reflected is smaller. Data recorded under clear sky conditions was excluded from this simulation. When no cloud description, but precipitation was observed, it was assumed, that the sky was mostly covered. The histograms for January and July of the refractivity differences for the different scenarios are shown in Figure 5.6.

In January there were 191 recorded values for clear sky conditions. Partly cloudy sky conditions were more frequent than cloudy sky conditions with 344 to 223 recorded values, respectively. For both scenarios small refractivity differences were clearly dominant, the occurrence of larger refractivities was decreasing fast. The two sky

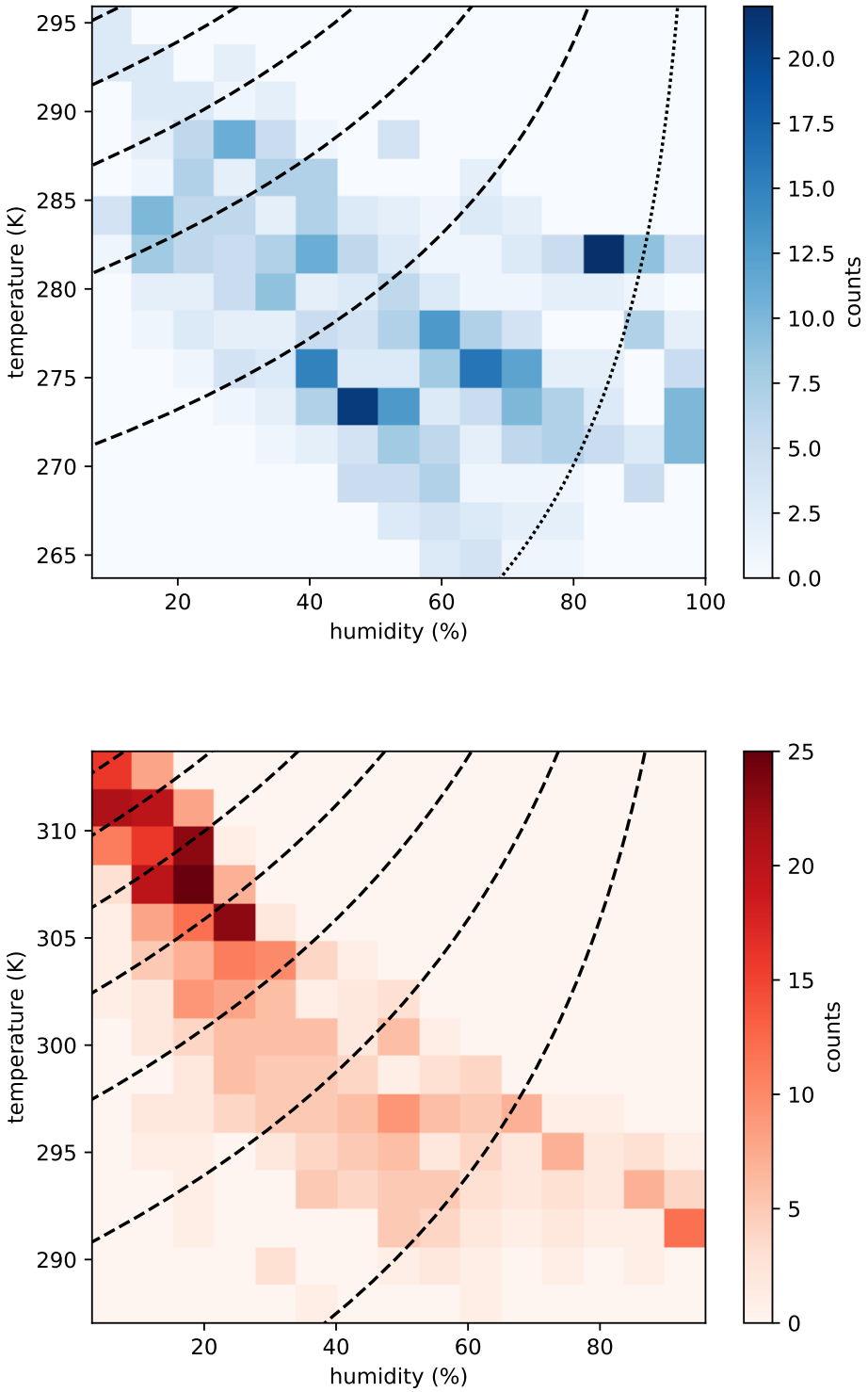

Fig. 5.5: Occurrence of temperature and humidity values in Bishop in January 2018 (top) and July 2018 (bottom) for cloudy and partly cloudy conditions combined. The dashed lines mark value combinations, which lead to the same refractivity difference. For January the distance between the equi-refractivity lines is 10 and the dotted line is a refractivity difference of 5, for July the distance between the lines is 20. Large refractivity difference values are in the upper left corner, low refractivity difference values are in the bottom right corner.

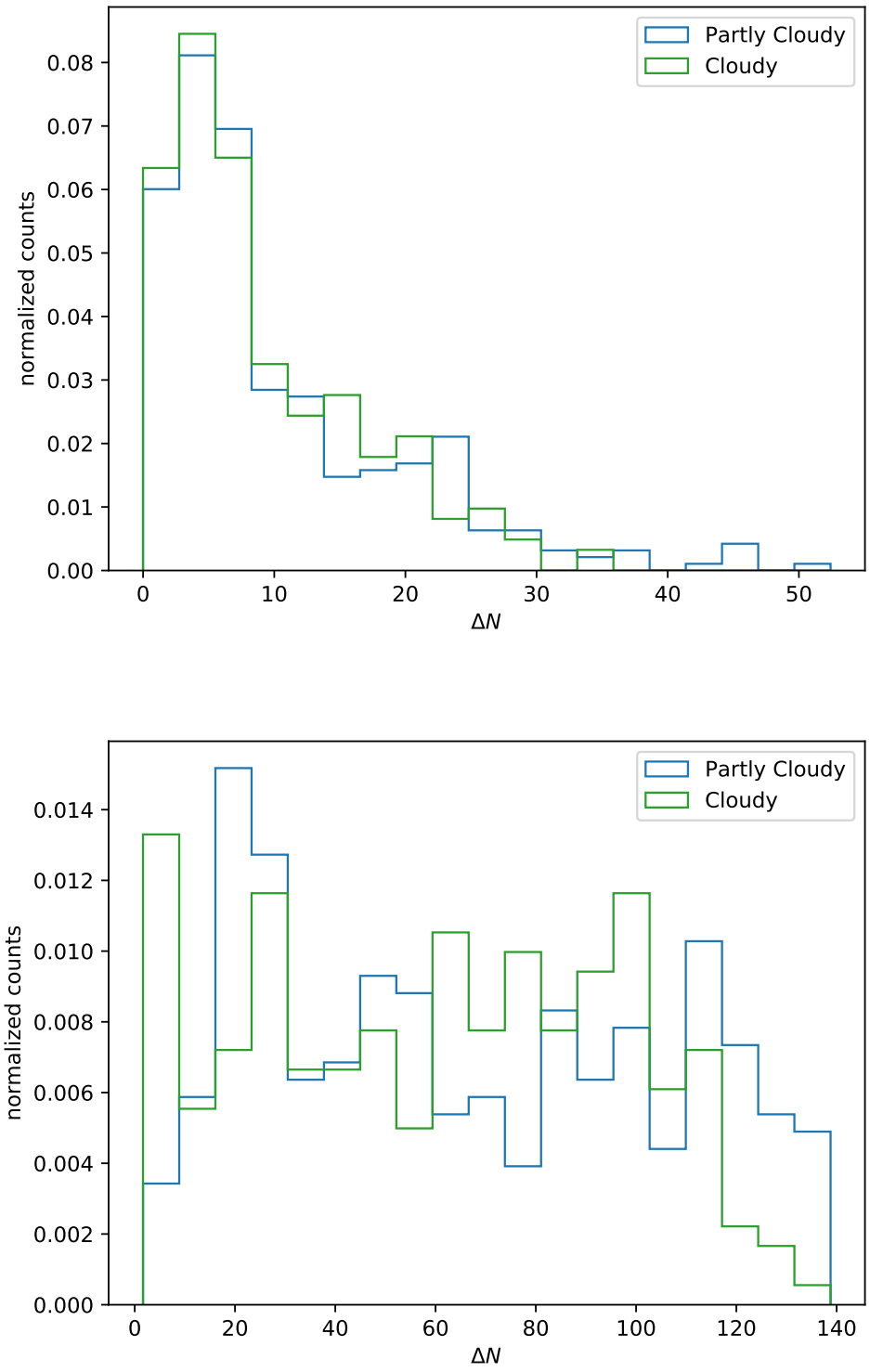

Fig. 5.6: Calculated occurrence of refractivity difference between $0.1\,\mathrm{m}$ inside the cloud layer and $0.1\,\mathrm{m}$ below the boundary for Bishop in January (top) and July (bottom) for cloudy and partly cloudy sky conditions.

conditions show a very similar distribution. In July clear skies were more frequent with 288 recorded values for clear sky conditions, and with 283 for a partly cloudy sky and 250 times for cloudy sky conditions these two conditions occurred about equally often. The range of refractivity differences is three times as large as the range in January and the values are uniformly distributed.

The reflected intensity is higher for higher refractivity differences, therefore higher background signals are expected in July. This is consistent with the observation of frequent occurrence of high temperatures and low humidity in July. At the same time, clouds are less likely to occur in July, which leads to more time without background reflections. To calculate the value of the reflected intensity, knowledge about the cloud height is required. Using the cloud height, the actual occurring refractivity difference can be calculated, the above histograms were calculated for a constant cloud height. The cloud height also determines the angle under which the ray is reflected, which is required to calculate the reflectivity.

5.2 Reflections as dependent on cloud height

The height of the cloud boundary layer has a strong influence on the intensity of a reflected ray: on one hand, the cloud height influences the refractivity difference between below and inside the cloud layer, see left part of Figure 5.7. At lower cloud heights the refractivity difference is larger, as the temperature is higher and the same relative humidity difference translates to a bigger water vapor pressure difference, see Figure 5.3. On the other hand, the cloud height determines the angle under which rays can be reflected into the detector for a fixed distance between source and detector, see equation 3.21. For low cloud heights, the reflection angle is large. The reflection angle determines the refractivity by the Fresnel equations. For large incident angles, corresponding to small elevation angles, the effective reflectivity is high, see the right part of Figure 5.7, where the logarithm of the effective reflectivity is shown. Furthermore, the cloud height determines the path length of the reflected ray, where longer paths leading to smaller intensities on arrival according to the propagation of a spherical wave.

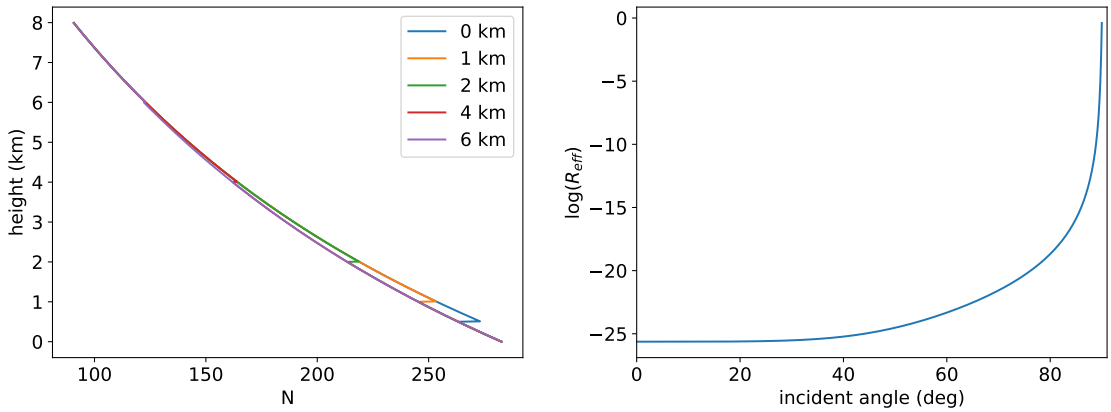

Fig. 5.7: Influence of the cloud height on the atmospheric refractivity profile (left) and logarithm of the reflectivity coefficient over the incident angle (right).

Again the propagation of a single ray from the source to the detector, reflected at a closed cloud layer, was simulated. When varying cloud height and temperature simultaneously, the highest reflected intensities were found for high temperature and low cloud altitudes, see Figure 5.8. At low cloud altitudes the slope of the lines of equal reflected intensity in units of $\mathrm{km/K}$ is very small, an increase of $1\,\mathrm{km}$ in cloud height leads to a larger decrease in intensity than a decrease of temperature of $10\,\mathrm{K}$. At higher altitudes the influence of the temperature increases. At low temperatures the intensity decrease with height is faster than at high temperatures. When varying cloud height and humidity, the highest reflected intensities were found for low humidity values and low cloud altitudes, see Figure 5.9. At humidity values below $90\,\%$ the cloud height has a significantly larger impact on the reflected intensity than the humidity. At values close to $100\,\%$ relative humidity, all lines are converging towards a vertical line, where the influence of the cloud height is very small as the logarithm of the relative intensity is diverging. With increasing cloud altitude the decrease in intensity with cloud altitude gets slower.

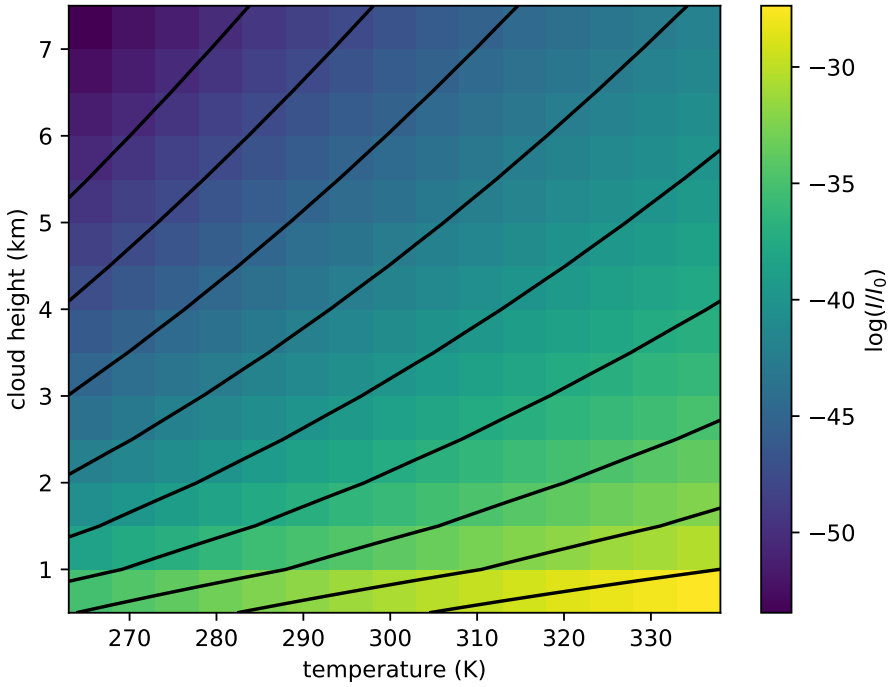

Fig. 5.8: Simulated logarithmic intensity of a ray reaching the detector by reflection on a cloud depending on the height of the cloud layer and temperature. The lines indicate parameter combinations with an equal simulated intensity value.

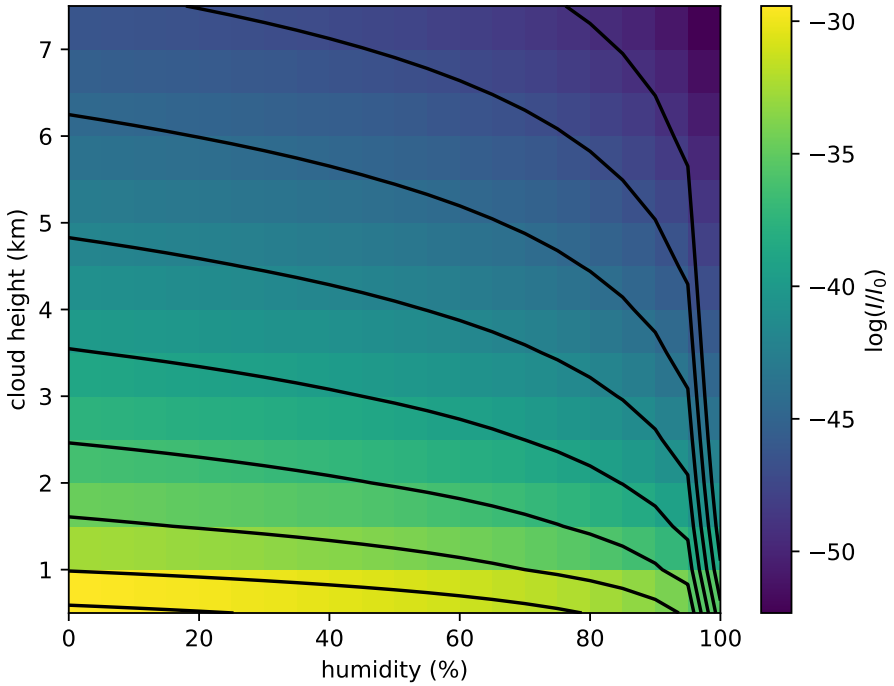

Fig. 5.9: Simulated logarithmic intensity of a ray reaching the detector by reflection on a cloud depending on the height of the cloud layer and humidity. The lines indicate parameter combinations with an equal simulated intensity value.

Using the cloud height data, also the most frequent elevation angles under which reflected rays are detected can be predicted. From the cloud height histogram, see Figure 4.5, elevation angle histograms are calculated. To study how much the rays reflected at different cloud heights contribute to a detected background, the weather conditions from the time of the cloud measurement were analyzed. Then the elevation angle histogram was weighted by the refractivity difference between below and inside the cloud, see the top of Figure 5.10, and weighted by the reflectivity at the cloud, see the bottom of Figure 5.10. When weighting with the refractivity difference, there are two peaks for January, one at $4°$ and one at $25°$. In July only one broad peak is visible, around $25°$. When considering the reflectivity as weight, only small angles are contributing, due to the strong influence of the angle on the resulting reflectivity, shown in Figure 5.7. This leads to a peak for January and July below $10°$.

It can be concluded that reflections on clouds can direct rays from the background source Bishop to the detector. Especially high background intensities are expected at high temperatures and low humidity as prevailing in summer. Lower cloud altitudes result in higher relative reflected intensities. The predicted reflected background is indeed peaked at certain elevation angles, as observed in the OVRO-LWA measurements, although the $15°$ elevation angle found in the measurements was not reproduced for January in the simulations. This will be discussed in Chapter 6. The angles under which high intensities are detected are dependent on cloud and weather conditions and are thus expected to change seasonally. This is in agreement with the continuous elevation angle region in which background signals were observed in the AERA measurements, see Figure 2.2, where the data was collected over nine months.

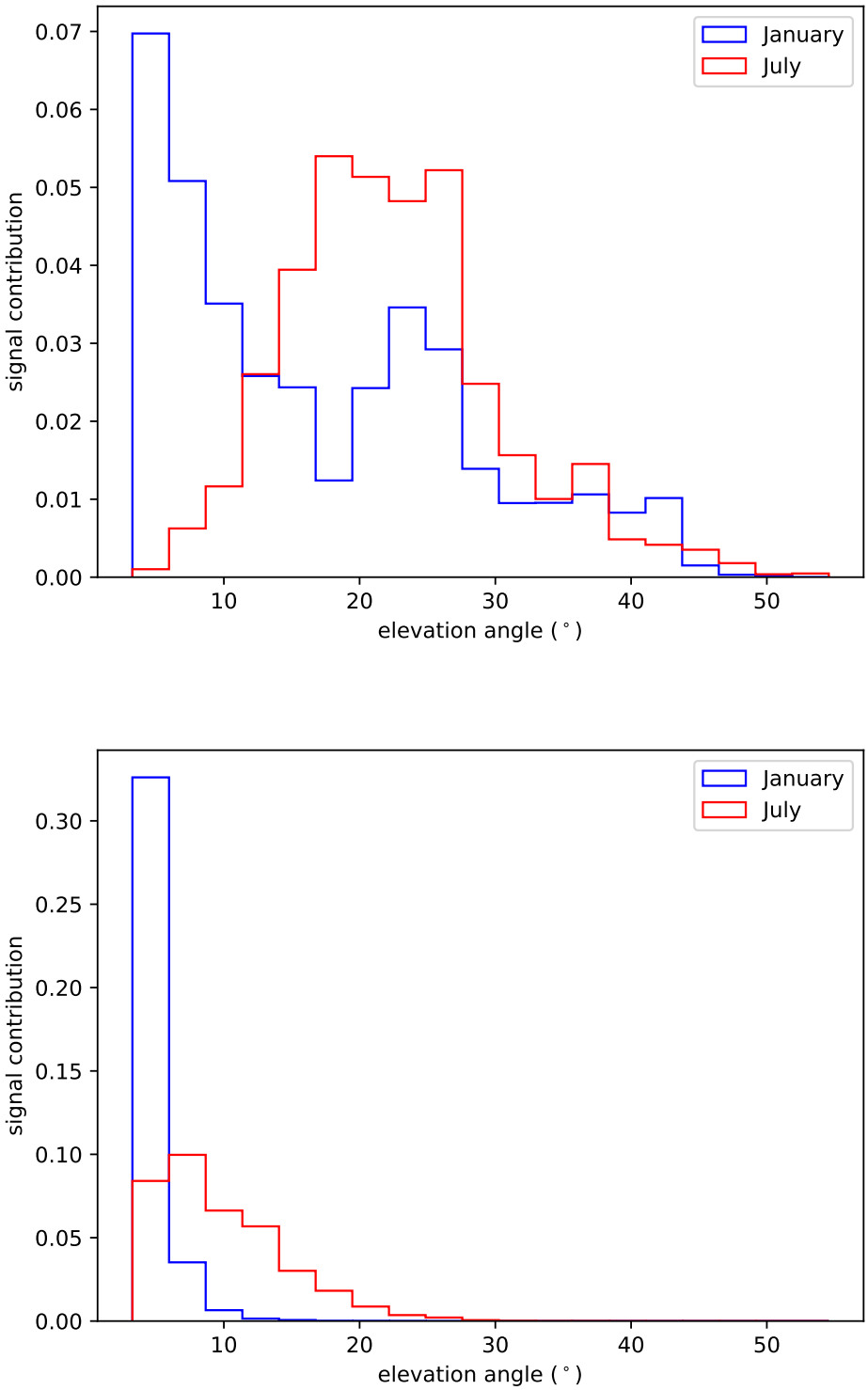

Fig. 5.10: Histograms of the elevation angle under which reflected rays reach the detector for January and July based on the analysis of one month of data (2018) of cloud heights from the CALIPSO mission. In the top histogram the elevation angles are weighted by the refractivity difference below and inside the cloud, calculated from weather data at the time of the CALIPSO data. In the bottom histogram the elevation angles are weighted by the reflectivity of the cloud boundary.

5.3 Atmospheric deflections

A different potential mechanism for noise reaching the detector at higher angles than from direct line-of-sight propagation, could be the deflection of radio rays in the atmosphere as it occurs during trapping conditions, see section 3.1. To study this propagation mechanism, the radio refractivity gradient has to be considered instead of the radio refractivity itself. The behavior of the gradient dependent on the parameters temperature, pressure, and humidity can be seen in Figure 5.11. When using the average annual weather conditions for Bishop, normal propagation conditions prevail. The gradient becomes larger negative with higher temperatures, higher atmospheric pressure, and higher humidity.

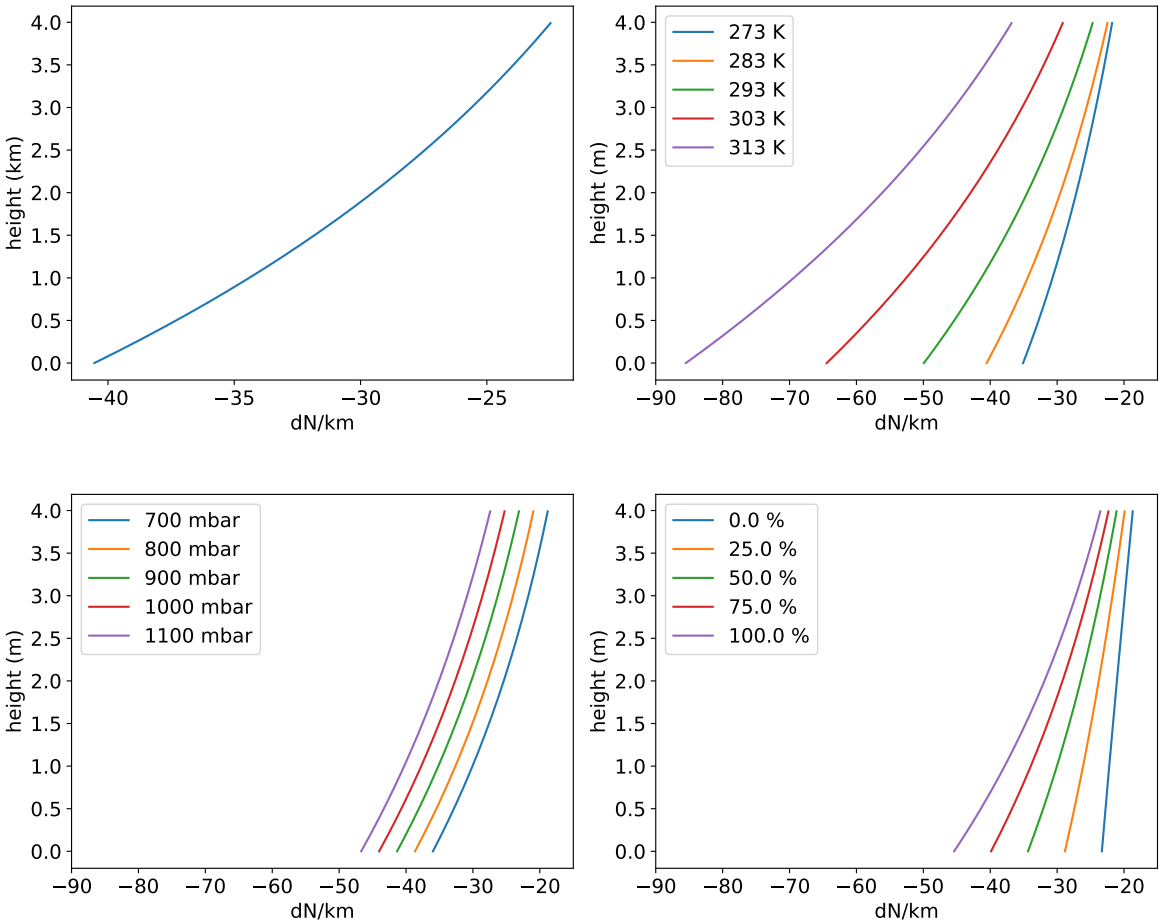

Fig. 5.11: Atmospheric refractivity gradient with annual average weather conditions of Bishop (upper left) and dependence of refractivity gradient on ground temperature (upper right), pressure (lower left), and humidity (lower right).

To determine how large the atmospheric refractivity gradient has to be for a ray to be bend back towards the Earth and reach the detector for the distance between detector and ray of $17.6\,\mathrm{km}$, rays were simulated in atmospheres with different constant refractivity gradients. For the elevation angle of the emitted ray at the source, a small angle of $5°$ was chosen, as for higher elevation angles, higher gradients are required to change the direction of the ray. In Figure 5.12 trajectories

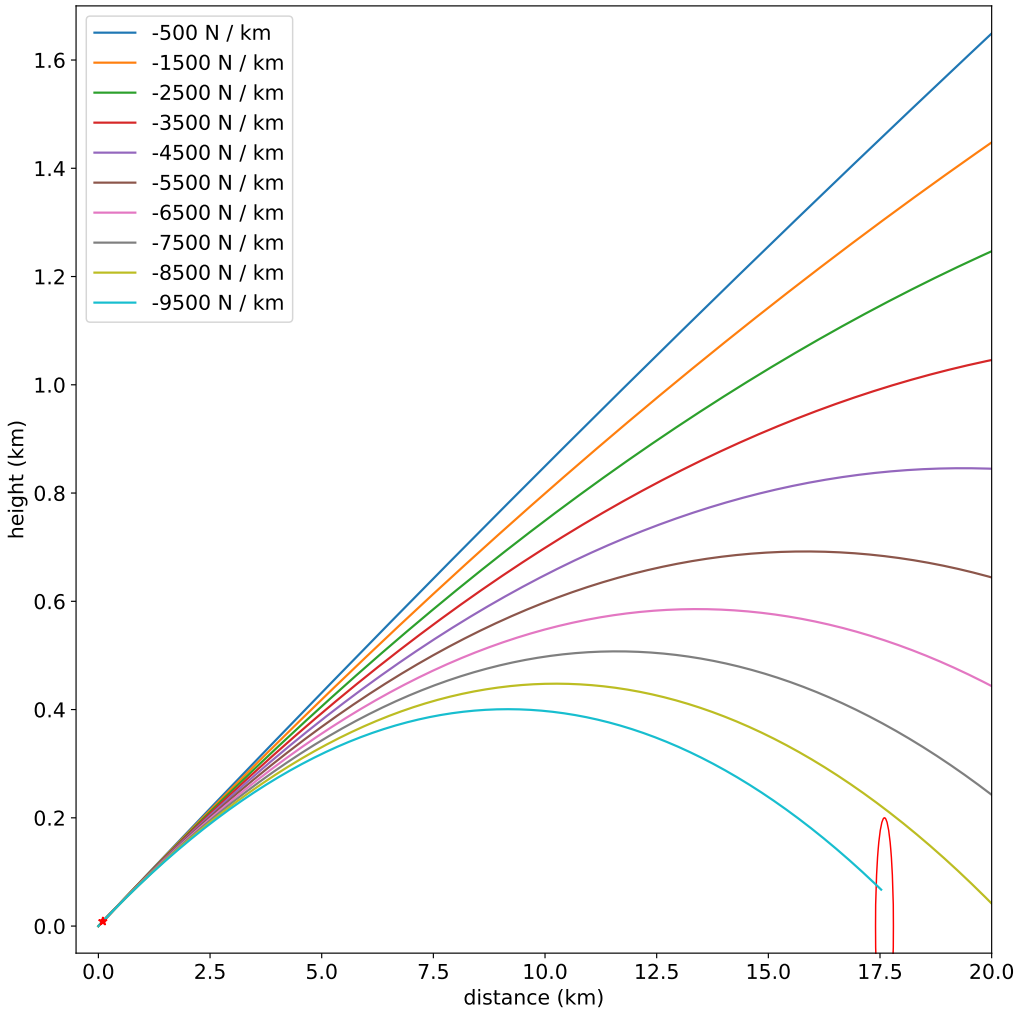

Fig. 5.12: Ray trajectory of rays emitted at an elevation angle of $5°$ with different atmospheric refractivity gradients. The detector is simulated as a sphere with $200\,\mathrm{m}$ radius.

for different values of the refractivity gradient can be seen. The value of the gradient, where the ray is deflected into the detector is with $-9500\,N\mathrm{km}^{-1}$ extremely high and even under very extreme weather conditions not reachable.

Horizontally emitted rays emitted in Bishop, lying $65\,\mathrm{m}$ higher than the OVRO-LWA, can reach the detector at much smaller refractivity gradients, see Figure 5.13. For this simulation, also the height change due to the curvature of the Earth of $24\,\mathrm{m}$ for $17.6\,\mathrm{km}$ has to be considered. The simulated detector here is a disk on the ground with a height of $2\,\mathrm{m}$ and a diameter of $200\,\mathrm{m}$. The required refractivity value of $-600\,N\mathrm{km}^{-1}$ is only reachable under extreme weather conditions. Additionally, the elevation angle measured at the detector with $0.5°$ is too small to explain the background signal. The OVRO-LWA self-trigger system would reject this signal.

It can be concluded that deflection in the atmosphere with a monotonous decreasing refractivity gradient cannot cause the observed background. This can change for so-called atmospheric ducts: due to temperature or humidity inversions the atmospheric

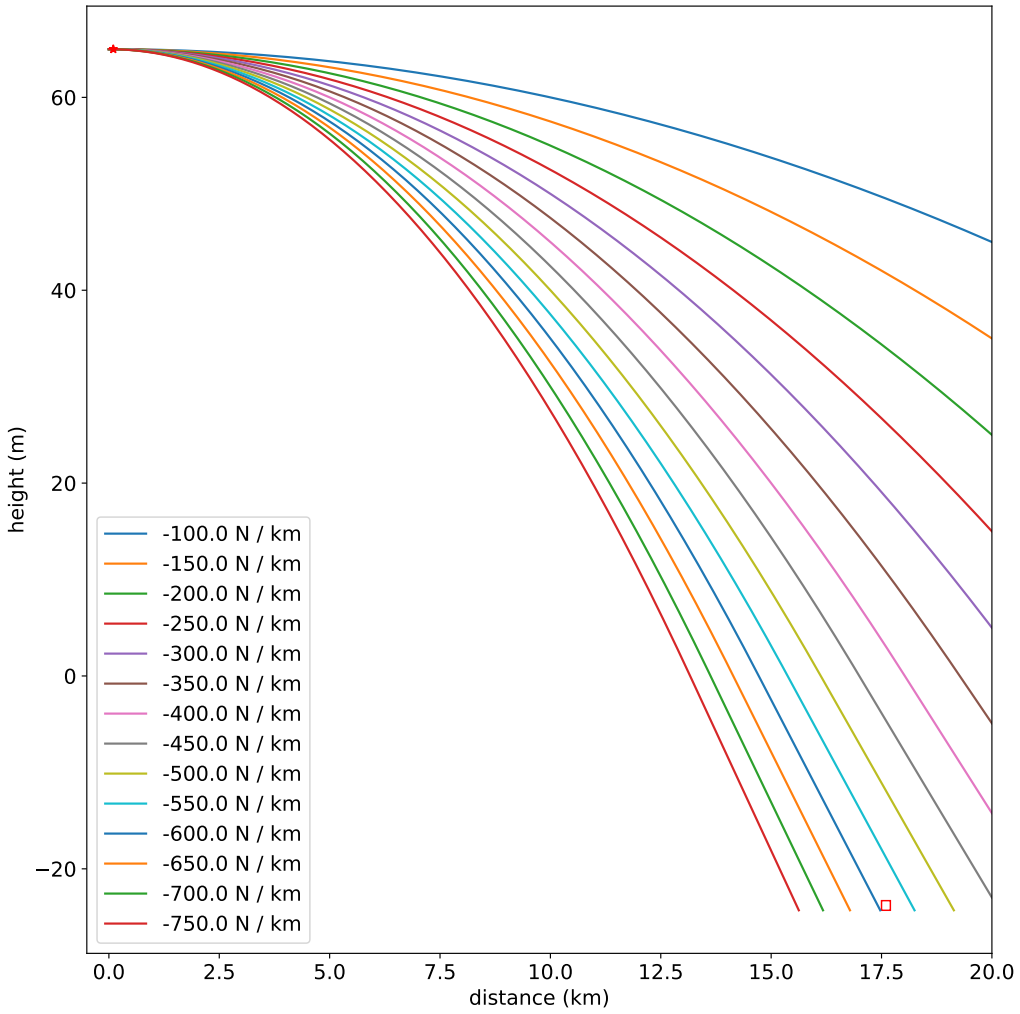

Fig. 5.13: Ray trajectory of rays emitted horizontally with different atmospheric refractivity gradients considering the topology between Bishop and the OVRO-LWA and the curvature of the Earth. The detector is simulated as a disk with a diameter of $200\,\mathrm{m}$ and a height of $2\,\mathrm{m}$.

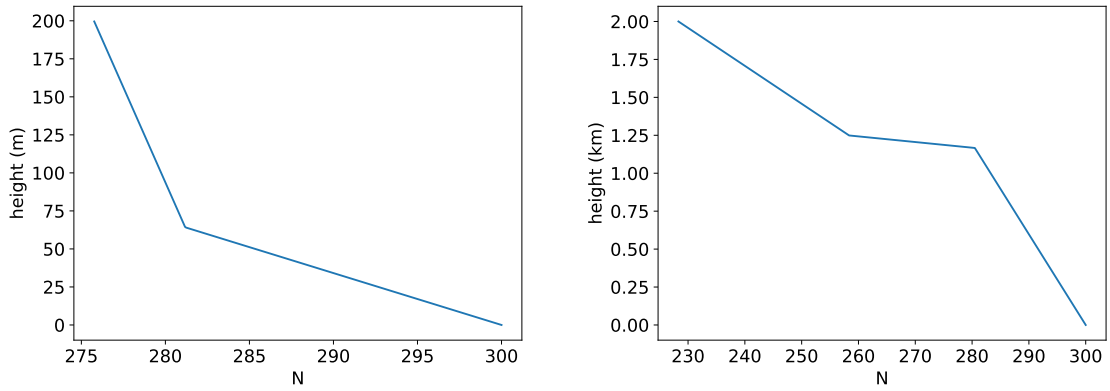

Fig. 5.14: Refractivity profile of a surface duct (left) and elevated duct (right) with the average thickness, height and strength for a location $18\,\mathrm{km}$ from Bishop. Data from [14].

refractivity is not continuous, the gradient changes discontinuously. The duct can change the direction of rays and reflect them back to Earth [36]. It is distinguished between surface ducts with the trapping layer on the surface and elevated ducts, where the trapping layer starts above the surface. From radiosonde data it is observed that surface ducts prevail $9.2\,\%$ of a year and elevated ducts $15.8\,\%$ of the year for a location $18\,\mathrm{km}$ Bishop. The average parameters for the ducts are shown in Figure 5.14. For both ducts, the propagation of radio rays was simulated, only slight differences from the regular propagation were observed, especially no bending of rays back to Earth was visible. More extreme ducts, which are able to bend radio noise back to the Earth could occur, but less likely for long enough to produce the prominent background signal, especially at an elevation angle of $15°$.

5.4 Predictions for OVRO-LWA measurement

As it was concluded that of the two considered mechanisms only the reflections on clouds are able to produce the observed background signal of the OVRO-LWA measurement, reflections on clouds were simulated with weather data from the days of measurement recorded at Bishop. Initially, a constant lower cloud boundary height of $2\,\mathrm{km}$ was assumed. The resulting reflectivity of the clouds calculated from the refractivity difference and the reflection angle, given by the fixed cloud height, can be seen in Figure 5.15. The expected relative intensity of the reflection is very small with maximal $2.5 \cdot 10^{-6}\,\%$. It can also be seen that the reflected intensity varies strongly over time. In the afternoon of the 8$^{\text{th}}$, noon of the 9$^{\text{th}}$ and 10$^{\text{th}}$, especially strong reflections are predicted, in the afternoon of the 9$^{\text{th}}$ and in the night to the 10$^{\text{th}}$ especially low reflections are predicted.

It was concluded earlier, that knowledge of the lower cloud boundary height is essential for a prediction of the reflected intensity. During the measurements at the OVRO-LWA, three overflights of CALIPSO gained cloud height data. As cloud conditions can change very quickly, and the data points are from different locations, this is not sufficient to give a prediction about the development of the reflected intensity under the influence of changing cloud height. However, to demonstrate the effect on the time behavior of reflected intensity simulated for a constant cloud height, the available measurement values were taken to construct a toy-model for the cloud height development. One measurement point had to be excluded as it was lower than $0.5\,\mathrm{km}$. It was assumed, that the two lower altitude values represent a lower cloud layer and the two larger altitude values represent a higher, second cloud layer. A linear change in cloud height was assumed between the measurement values. With the time-dependent cloud height as input, the simulations were repeated, see Figure 5.16. Contributions from the second, higher cloud layer were 6 orders of magnitude smaller than from the first layer, therefore only reflections from the lowest layer are shown here. The reflections are significantly larger than in the simulation before, as the altitude of the lower cloud layer is mostly lower than $2\,\mathrm{km}$. The general reflectivity trend stays the same, as in the prediction with a constant cloud height, but the maxima, where the cloud altitude is low, become more prominent than before. But this trend can change drastically if the cloud height follows a more complex function.

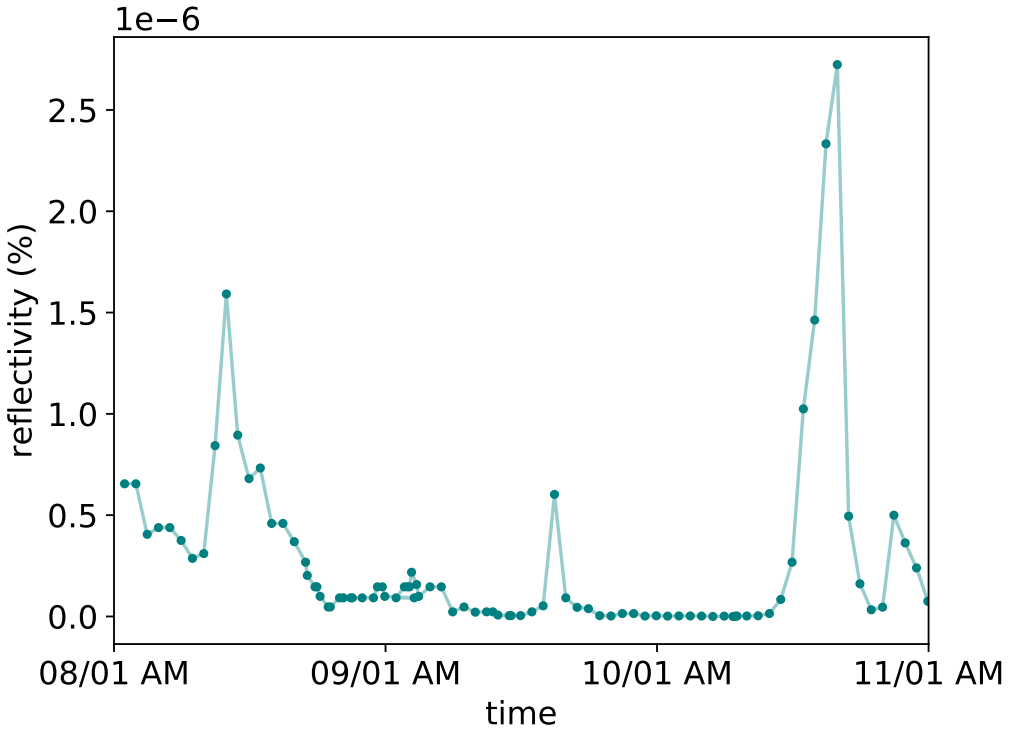

Fig. 5.15: Simulated cloud reflectivity during the three days of measurement at the OVRO-LWA. The reflectivity was calculated from local weather data. A closed cloud cover with the lower boundary at a constant height of $2\,\mathrm{km}$ was assumed.

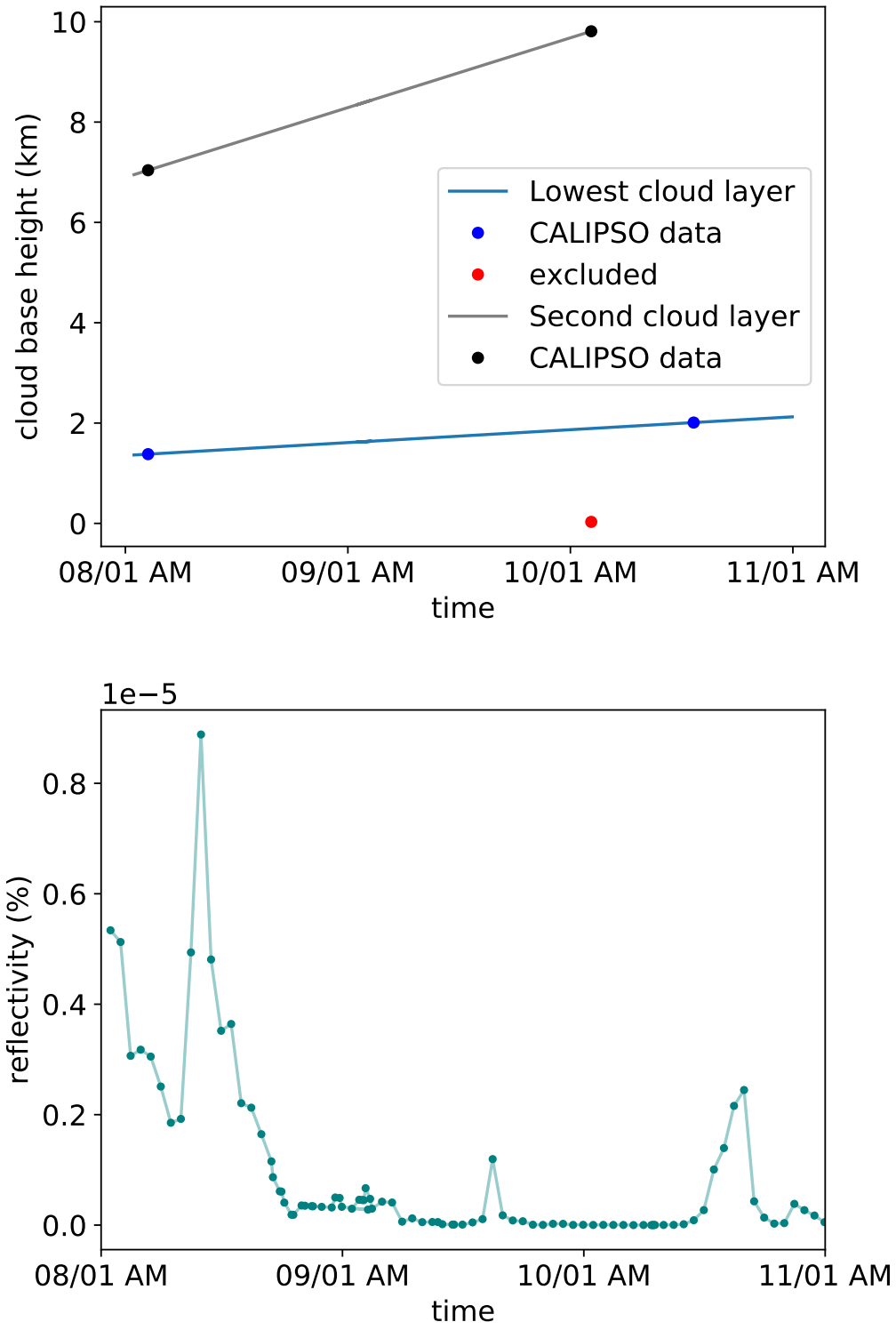

Fig. 5.16: Assumed cloud height development over the time of the measurement at OVRO-LWA based on three measurements of cloud height (top) and time dependence of cloud reflectivity (bottom) based on local weather data and the lower cloud boundary height profile.

The shown predicted time evolution of the reflectivity could now be compared with the time evolution of the measured background to investigate if the here presented model can explain the observed background. But background data at a smaller time resolution than presented in Figure 2.1, which shows the cumulative background over the full time of the measurement, is not available for the measurement in 2018 and currently data taking is not possible due to an ongoing upgrade to a larger array.

6 Discussion and Conclusion

In this thesis, I investigated if the radio noise measured at OVRO-LWA at elevation angles over the horizon could be caused either by reflections on clouds or deflection in the atmosphere.

To simulate propagation in the atmosphere, the atmospheric refractivity dependent on height is required, which can be calculated from an empirical formula depending on pressure, temperature, and relative humidity. The assumed height dependent curves of these parameters were compared to averaged monthly measured values for January and July at different altitudes in the atmosphere, as well as the refractivity calculated from the model based on values measured at the ground and the refractivity calculated from the measured parameters at each height. Overall a good agreement was found, especially in January. This agreement leads to the assumption that weather data taken at the ground is suited as input for the simulations.

The reflection of rays on clouds was simulated for different weather conditions, where clouds were modeled as sections of the atmosphere with 100% relative humidity. It was found that the reflected relative intensity is independent of the air pressure. For higher temperatures and lower humidity values on the ground, higher reflections are predicted. Lower altitudes of the cloud base, where the reflection takes place, lead to higher reflected intensities.

The two parameters determining the reflectivity of clouds are the refractivity difference between in and below the cloud and the angle of the incident ray on the cloud, given by the cloud height, which also determines the elevation angle, under which the reflected ray is detected. Therefore the incidence of these parameters was investigated for January and July from local weather recordings and CALIPSO satellite data to gain information about cloud height. In January significantly lower refractivity differences were found than in July, where the range of resulting refractivity difference values was three times as large and the values were uniformly distributed over the whole range and not peaked at low values as in January. Therefore stronger background signals are expected in July.

The cloud height data was used to create distributions of the elevation angle, under which a detected ray would appear. Two measures to evaluate how strong the reflected ray would contribute to the detected background, given the weather conditions prevailing during the cloud height measurements, were introduced: the refractivity difference and the reflectivity, compare Figure 5.10 top (refractivity difference) and bottom (reflectivity). The histogram weighted by the refractivity difference shows two peaks for January at $4°$ and $25°$, for July one broader peak around $20°$ appears. When weighting the elevation angle distribution with the reflectivity, the rays at larger elevation angles are contributing less.

The refractivity difference is not fully suitable to describe the intensity of the reflected ray at the detector as the absolute refractivity and angle of the incoming ray is not taken into consideration. Both are included in the reflectivity. However, this value is calculated under the assumption, that the cloud boundary layer is abrupt and completely straight. The dependence of the intensity on the incoming angle is stronger than the dependence on any other parameter. This cannot be justified as the lower boundary layer of clouds can be quite irregular. Deeper insights into the structure of clouds and a comparison to measurement data, for instance, the reflected intensity of a lidar, are required to find the right measure to translate cloud height data into expected intensities at the detector.

For both weighted histograms a discrepancy between the predicted elevation angle distribution for January and the directions recorded in the measurement with a peak at $15°$ was found. But the data used in this analysis is not suited for a precise prediction of the OVRO-LWA background. For the days of the measurement, not enough cloud data are available to predict the direction of the strongest background. As the elevation angle histograms were created with cloud data from an area of $500\,\mathrm{km} \times 500\,\mathrm{km}$ around Bishop, local conditions are not represented in detail. The cloud data of January stems from 18 overflights on 10 days of January 2018. It is uncertain how well this data set represents the conditions during the measurement. Additional discrepancies could be caused by a mismatch between the layer detection of the CALIPSO satellite, which is conducted by an optical measurement, and the boundary, where the radio reflection takes place. Furthermore, in the simulations, a constant relative humidity is assumed, but in the vertical profiles, it was visible, that the humidity has a very complex profile, but decreases towards large heights. This leads to a larger refractivity difference at higher altitudes than assumed in the simulation. Considering the humidity profile in a suitable model could therefore shift the distribution of expected elevation angles towards higher angles.

The resulting reflectivity values are generally small, with $2.5 \cdot 10^{-5}\%$ as the predicted maximal reflection intensity for the days of the measurement at OVRO-LWA in January 2018, but a cities contain multiple and very strong radio sources, is is possible, that the small relative intensities of reflected rays lead to a significant noise source.

For the second possible mechanism, the atmospheric deflection of rays, it was concluded that it cannot be the cause of the radio noise. The atmospheric refractivity gradient required to bend rays, emitted at angles above the horizon, back to the detector over the distance between Bishop and the OVRO is one order of magnitude too high to occur even under extreme weather conditions. Also, potential atmospheric ducts, simulated with average parameters for Bishop, were found to be not able to deflect the rays towards the detector. However, as only the average parameters for the ducts are known, ducts, that would cause a radio noise signal in the detector could occur. If they are occurring, it is likely, that they are only contributing, but not the main origin of the background as ducts prevail infrequently over continental areas. Detailed atmospheric data for this region is required before drawing a final conclusion. Additionally, the study of ducts in a wave propagation model instead of a ray model could be insightful [38].

Overall, it can be concluded that the reflections of radio noise on clouds could possibly cause the background signals peaked at certain elevation angles, observed in several experiments. A comparison of the simulations to measured background noise with parallel supervision of atmospheric parameters is now necessary to test the validity of the predictions presented here. This was not possible for the past measurement as no background data plots for smaller time intervals were created and the whole background data is not available anymore.

As a starting point for the comparison, the background signal intensity and elevation angle can be determined during a future run of the OVRO-LWA. The intensity and angle development over time can be compared with changes in the predicted reflected intensity depending on measured ground temperature and humidity, as well as sky conditions. Measurements on a clear day should show significantly less background signal than on cloudy days. The knowledge of the cloud base altitude is crucial for further testing of the predictions. For the same cloud altitude, less background is expected on colder days. An initial approach could be to use measurement data from days, were two overflights of the CALIPSO mission took place. There are other satellite missions taking cloud height data, e.g. CloudSAT, MODIS, CLARA-A2 [37], which could be used to increase the number of known cloud heights, but their data could not be accessed during this thesis.

Additional precision and more measurement points could be gained if a ceilometer for ground-based cloud height measurements is used at the location of the antenna array. If the here described model for cloud reflections shows to be precise in describing the background noise, the ceilometer in combination with a weather station can help to suppress the reflected background without completely rejecting signals from the direction of a city, which increases the detection efficiency. To improve background predictions for the location of the array regular measurements with a radiosonde could be performed to create vertical atmosphere profiles. Further analysis of the background noise is required to search for additional or alternative effects contributing to the background signal.

Bibliography

[1] Alessandro De Angelis and Mário Pimenta. *Introduction to particle and astroparticle physics: multimessenger astronomy and its particle physics foundations*. Springer, 2018.

[2] Frank G Schröder. „Radio detection of cosmic-ray air showers and high-energy neutrinos“. In: *Progress in Particle and Nuclear Physics* 93 (2017), pp. 1–68.

[3] Tim Huege. „Radio Detection of Cosmic Rays–Achievements and Future Potential“. In: *Proceedings of 2016 International Conference on Ultra-High Energy Cosmic Rays (UHECR2016)*. 2018, p. 011031.

[4] Stefan Fliescher. „Antenna devices and measurement of radio emission from cosmic ray induced air showers at the Pierre Auger Observatory“. In: (2011).

[5] Jörg R Hörandel. „Status and perspectives of the radio detection of highenergy cosmic rays“. In: *EPJ Web of Conferences*. Vol. 209. EDP Sciences. 2019, p. 01051.

[6] Ryan Monroe, Andres Romero Wolf, Gregg Hallinan, et al. „Self-triggered radio detection and identification of cosmic air showers with the OVRO-LWA“. In: *Nuclear Instruments and Methods in Physics Research Section A: Accelerators, Spectrometers, Detectors and Associated Equipment* 953 (2020), p. 163086.

[7] Jaime Alvarez-Muñiz, Washington R. Carvalho, and Enrique Zas. „Monte Carlo simulations of radio pulses in atmospheric showers using ZHAireS“. In: *Astroparticle Physics* 35.6 (2012), pp. 325–341.

[8] Enrique Zas. „Neutrino detection with inclined air showers“. In: *New Journal of Physics* 7 (May 2005), pp. 130–130.

[9] Marta Trini. „Ultra-high energy neutrinos searches with the Pierre Auger Observatory“. In: *SciPost Physics Proceedings* 1 (2019), p. 047.

[10] Michael W. Eastwood, Marin M. Anderson, Ryan M. Monroe, et al. „The Radio Sky at Meter Wavelengths: m-mode Analysis Imaging with the OVRO-LWA“. In: *The Astronomical Journal* 156.1 (June 2018), p. 32.

[11] Tobias Winchen. „RadioPropa — A Modular Raytracer for In-Matter Radio Propagation“. In: *EPJ Web of Conferences* 216 (2019). Ed. by G. Riccobene, S. Biagi, A. Capone, C. Distefano, and P.Editors Piattelli, p. 03002.

[12] Yuefei Zeng, Ulrich Blahak, Malte Neuper, and Dorit Jerger. „Radar beam tracing methods based on atmospheric refractive index“. In: *Journal of Atmospheric and Oceanic Technology* 31.12 (2014), pp. 2650–2670.

[13] International Telecommunication Union. *Effects of tropospheric refraction on radiowave propagation*. Recommendation ITU-R P.834-8. 2016.

[14] International Telecommunication Union. *The radio refractive index: its formula and refractivity data*. Recommendation ITU-R P.453-14. 2019.

[15] Arden L Buck. „New equations for computing vapor pressure and enhancement factor“. In: *Journal of applied meteorology* 20.12 (1981), pp. 1527–1532.

[16] D. M. Murphy and T. Koop. „Review of the vapour pressures of ice and supercooled water for atmospheric applications“. In: *Quarterly Journal of the Royal Meteorological Society* 131.608 (2005), pp. 1539–1565. eprint: https://rmets.onlinelibrary.wiley.com/doi/pdf/10.1256/qj.04.94.

[17] International Telecommunication Union. *Reference standard atmospheres*. Recommendation ITU-R P.835-6. 2017.

[18] Mário N Berberan-Santos, Evgeny N Bodunov, and Lionello Pogliani. „On the barometric formula“. In: *American Journal of Physics* 65.5 (1997), pp. 404–412.

[19] John David Jackson. *Classical Electrodynamics*. 3rd ed. Wiley, 1998.

[20] Natasha L. Miles, Johannes Verlinde, and Eugene E. Clothiaux. „Cloud Droplet Size Distributions in Low-Level Stratiform Clouds“. In: *Journal of the Atmospheric Sciences* 57.2 (2000), pp. 295–311.

[21] Andrew J. Heymsfield, Carl Schmitt, and Aaron Bansemer. „Ice Cloud Particle Size Distributions and Pressure-Dependent Terminal Velocities from In Situ Observations at Temperatures from 0° to -86°C“. In: *Journal of the Atmospheric Sciences* 70.12 (2013), pp. 4123–4154.

[22] Wolfgang Demtröder. *Electrodynamics and Optics*. Springer, 2019.

[23] Earl E Gossard and Richard G Strauch. „The refractive index spectra within clouds from forward-scatter radar observations“. In: *Journal of Applied Meteorology* 20.2 (1981), pp. 170–183.

[24] Marcelo Alonso and Edward Finn. *Fundamental University Physics Volume II Fields and Waves*. Addison-Wesley, 1975.

[25] Google Earth. *Owens Valley N* $37°17'44.39''$ *W* $118°20'49.04''$. Image Date 7/17/2016, View altitude $26.09\,\mathrm{km}$.

[26] Pablo Aparicio Ruiz, Rosa Schiano-Phan, and José Salmerón. „Climatic applicability of downdraught evaporative cooling in the United States of America“. In: *Building and Environment* 136 (Mar. 2018).

[27] Stephen D Burk and William T Thompson. „The summertime low-level jet and marine boundary layer structure along the California coast“. In: *Monthly weather review* 124.4 (1996), pp. 668–686.

[28] International Telecommunication Union. *Software, Data and Validation examples for ionospheric and tropospheric radio wave propagation and radio noise: Atmospheric profile data*. URL: https://www.itu.int/en/ITU-R/study-groups/rsg3/Pages/iono-tropo-spheric.aspx.

[29] Murry L. Salby. *Physics of the Atmosphere and Climate*. 2nd ed. Cambridge University Press, 2012.

[30] Christian Rolland. „Spatial and Seasonal Variations of Air Temperature Lapse Rates in Alpine Regions“. In: *Journal of Climate* 16.7 (2003), pp. 1032–1046.

[31] Weather Underground. *Bishop, CA Weather History*. URL: https://www.wunderground.com/history/daily/us/ca/bishop/KBIH.

[32] Pocatello Weather Forecast Office. *National Weather Service Information and Services Guide - Weather, Water and Climate*. 2012.

[33] Sunny Sun-Mack, Patrick Minnis, Yan Chen, et al. „Integrated cloud-aerosol-radiation product using CERES, MODIS, CALIPSO, and CloudSat data“. In: *Remote Sensing of Clouds and the Atmosphere XII*. Vol. 6745. International Society for Optics and Photonics. 2007, p. 674513.

[34] David Winker. *CALIPSO LID L2 01kmCLay-ValStage1 HDF File - Version 3.01*. 2010.

[35] Charles R. Trepte. *CALIPSO: Data User's Guide - Data Product Descriptions - Lidar Level 2 Cloud and Aerosol Layer Products*. 2019. URL: https://www-calipso.larc.nasa.gov/resources/calipso_users_guide/data_summaries/layer/index.php#dq.

[36] Ergin Dinc and Ozgur B Akan. „Beyond-line-of-sight communications with ducting layer“. In: *IEEE Communications Magazine* 52.10 (2014), pp. 37–43.

[37] Claudia J. Stubenrauch, William B. Rossow, Stefan Kinne, et al. „Assessment of global cloud datasets from satellites: Project and database initiated by the GEWEX radiation panel“. In: *Bulletin of the American Meteorological Society* 94.7 (2013), pp. 1031–1049.

[38] Yung-Hsiang Chou and Jean-Fu Kiang. „Ducting and turbulence effects on radio-wave propagation in an atmospheric boundary layer“. In: *Progress In Electromagnetics Research* 60 (2014), pp. 301–315.

Eigenständigkeitserklärung

Hiermit bestätige ich, dass ich diese Arbeit selbstständig und nur unter Verwendung der angegebenen Hilfsmittel angefertigt habe.

Ulm, den 01.04.2020 Carina Kanitz